Dynamics of episodic and continuous rhythmic activities from a developing central pattern generator

Simon A. Sharples [1,2,*], Alex Vargas [3,*], Adam P. Lognon[1,2], Leanne Young [4], Anchita Shonak [1,2], Gennady S. Cymbalyuk [3,5,+], and Patrick J. Whelan [1,2,4,+]

[1] Hotchkiss Brain Institute, University of Calgary, Calgary, AB, Canada; [2] Department of Neuroscience, University of Calgary, Calgary, AB, Canada; [3] Neuroscience Institute, Georgia State University, Atlanta, GA, USA; [4] Department of Comparative Biology and Experimental Medicine, University of Calgary, Calgary, AB, Canada; [3] Department of Physics and Astronomy, Georgia State University, Atlanta, GA, USA.
*, +, indicate equal contributors

Abstract: Developing spinal motor networks produce a diverse array of outputs, including episodic and continuous patterns of rhythmic activity. Variation in excitability state and neuromodulatory tone can facilitate transitions between episodic and continuous rhythms; however, the intrinsic mechanisms that govern these rhythms and transitions are poorly understood. Here, we tested the capacity of a single central pattern generator (CPG) circuit with tunable properties to generate multiple outputs. To address this, we deployed a computational model composed of an inhibitory half-centre oscillator. We tested the contributions of key properties predicted by the model to the generation of an episodic rhythm produced by isolated spinal cords of the newborn mouse. The model was capable of reproducing the diverse state-dependent rhythms evoked by dopamine in the neonatal mouse spinal cord. In the model, episodic bursting depended predominantly on the endogenous oscillatory properties of neurons, with persistent Na^+(I_{NaP}), Na^+-K^+ ATPase pump (I_{Pump}), and hyperpolarization-activated currents (I_h) playing key roles. Modulation of all three currents produced transitions between episodic and continuous rhythms and silence. Pharmacological manipulation of these properties in vitro led to consistent changes in spinally generated rhythmic outputs elicited by dopamine. The model also showed multistable zones within a narrow range of parameter space for I_{Pump} and I_h, where switches between rhythms were rapidly triggered by brief but specific perturbations. Outside of those zones, brief perturbations could reset episodic and continuous rhythmicity generated by the model. Our modelling and experimental results provide insight into mechanisms that govern the generation of multiple patterns of rhythmicity by a single CPG. We propose that neuromodulators alter circuit properties to position the network within regions of state-space that favour stable outputs or, in the case of multistable zones, facilitate rapid transitions between states.

Keywords: dopamine, episodic rhythms, central pattern generator, spinal cord, rhythmicity, coexistence, multistability

Significance statement: The ability of a single CPG to produce and transition between multiple rhythmic patterns of activity is poorly understood. We deployed a complementary computational half-centre oscillator model and an isolated spinal cord experimental model to identify key currents whose interaction produced episodic and continuous rhythmic activity. Combined, our experimental and modelling approaches suggest mechanisms that govern generating and transitioning between diverse rhythms in mammalian spinal networks. This work sheds light on the ability of a single CPG to produce episodic bouts often observed in behavioural contexts.

Introduction

Locomotor behaviours enable organisms to navigate and interact with their environment. These behaviours are remarkably diverse and flexible, but many species share a defined set of locomotor acts that are often engaged in specific contexts. For example, locomotor behaviour during foraging is often episodic, interspersed with periodic pauses to survey the environment. In contrast, pauses are less favourable during migratory locomotor behaviours, which are generally continuous to maximize distance travelled. Animals also need the capacity to rapidly switch between locomotor behaviours. When foraging animals sense a predatory threat, they need to respond quickly by initiating a freeze or escape response (Ferreira-Pinto et al., 2018; Kim et al., 2017). In mammals, the neural mechanisms that govern the generation of episodic and continuous locomotor bursts and transitions between them are unclear, but studies in fish and *Xenopus* tadpoles offer some clues (Berg et al., 2018; Eaton et al., 2001; Sillar and Robertson, 2009).

Mounting evidence suggests that the spinal central pattern generator (CPG) encodes episodic and continuous locomotor patterns. Episodic and continuous patterns of rhythmicity can be generated in vitro in neonatal mouse, zebrafish, and *Xenopus* tadpole spinal cord preparations by varying their neuromodulatory tone and excitability state (Gozal et al., 2014; Marchetti and Nistri, 2001; McDearmid and Drapeau, 2006; Picton et al., 2018; Sharples and Whelan, 2017; Wiggin et al., 2012). In larval zebrafish, features of episodic locomotor behaviours change during development from long, sporadic swimming episodes to shorter episodes with a more regular beat-and-glide pattern (Buss and Drapeau, 2001; Lambert et al., 2012). This switch, which coincides with the onset of foraging behaviours (Borla et al., 2002), is mediated by D_4 dopamine receptors (Lambert et al., 2012) and patterns continue to mature through juvenile and adult stages of development (Gabriel et al., 2011; Müller et al., 2000). A similar developmental switch in locomotor behaviour has been reported in *Xenopus* tadpoles. During early developmental stages, D_2 dopamine receptors promote a sessile behaviour, and at later stages D_1 receptors facilitate episodic swimming for filter feeding (Clemens et al., 2012; Picton and Sillar, 2016). Swimming episodes in tadpoles have been linked to the activity-dependent Na^+-K^+ ATPase pump current (I_{Pump}; Zhang et al., 2015; Zhang and Sillar, 2012), which interacts with hyperpolarization-activated cation currents (I_h) and A-type K^+ currents (I_{KA}) in excitatory rhythm-generating interneurons (Picton et al., 2018; Zhang et al., 2015).

The circuit dynamics that produce these two network outputs and the mechanisms that drive transitions between patterns are less clear. One possibility is that disparate subcircuits generate different locomotor patterns (Li et al., 2007) and recruit respective circuit elements to enable transitions between patterns in animals such as mollusc (Arshavsky YuI et al., 1989, 1985), leech (Briggman and Kristan, 2006), *Xenopus* (W.-C. Li et al., 2007), and turtle (Berkowitz, 2010; Hao et al., 2011). Multiple patterns may also be generated by a single

multifunctional circuit with tunable properties (Berkinblit et al., 1978; Bondy et al., 2016; Getting, 1989; Gutierrez et al., 2013; Gutierrez and Marder, 2013; Mackie and Meech, 1985; Meech and Thomas, 1977; Parker et al., 2018). In support of this notion, we previously described a dynamic mechanism and developed a model of a single half-centre oscillator (HCO) that could produce two rhythmic patterns with very distinct cycle periods (CPs): a slow locomotor-like pattern (~ 1 s) and a fast paw-shake-like pattern (~ 0.1 s; Parker et al., 2018).

Here, we explored cellular dynamics that enable a single CPG to produce very slow episodic patterns of rhythmicity (episode period [EP] ~100 seconds) and identified changes in intrinsic properties that elicit transitions to faster continuous rhythmicity (CP ~ 1 s). We adapted our established biophysical model (Parker et al., 2018) to produce episodic and continuous patterns of rhythmic activity, similar to patterns previously observed in isolated newborn rodent spinal cord in vitro (Barbieri and Nistri, 2001; Gozal et al., 2014; Marchetti and Nistri, 2001; Sharples and Whelan, 2017). We then compared the contribution of key intrinsic properties predicted by the model to the generation of episodic rhythmicity elicited by dopamine in experiments on isolated neonatal mouse spinal cords. The isolated spinal cord of the neonatal mouse offers a convenient preparation to study these dynamics because episodic and continuous patterns can be elicited in vitro (Sharples and Whelan, 2017), and its cellular properties can be readily manipulated. Our complementary approaches provide novel insights into how CPGs produce multiple rhythmic patterns and transitions between them. We found that this capacity is accommodated not only through modulation of cellular properties, but also by incorporating multistable zones that afford rapid switching between patterns when triggered by brief, but specific inputs. Some of these results have been presented previously in abstract form (Vargas A & Cymbalyuk G, 2019).

Results

A biophysical model that generates episodic rhythmicity

We developed a biophysical model consisting of two neurons representing mutually inhibiting neuronal populations, an HCO. Our goal was to elucidate a mechanism that explains how a single oscillator generates episodic and continuous bursting, and then examine the model's output compared with experimental data. We suggest that the dynamics of episodic bursting rely on the interaction of persistent Na^+ current (I_{NaP}), I_{Pump}, and I_h. We validated predictions from the model using an isolated spinal cord preparation, in which we elicited episodic rhythmicity by bath application of dopamine (Supplemental Figure 1A, B). This preparation also allowed us to manipulate and assess the relative contribution of key properties predicted by the model to network operation. Note that similar forms of episodic rhythmicity are not exclusive to dopamine application; they can be evoked by trace amines (Gozal et al., 2014) and activation of excitatory tachykinin receptors (Barbieri and Nistri, 2001; Marchetti and Nistri, 2001) in neonatal mouse and rat spinal cord. Further, episodic rhythms generated in vitro display consistent temporal properties to swim episodes in

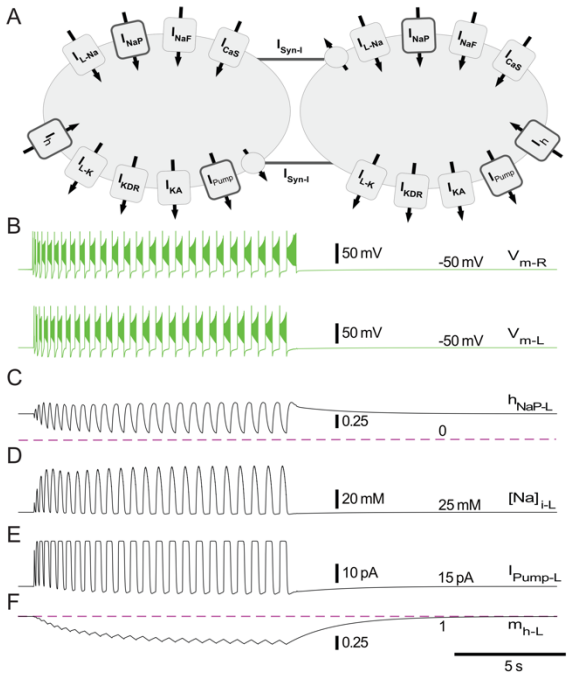

Figure 1: Dynamic interaction of the I_{NaP}, I_{Pump}, and I_h produce episodic bursting in a computational model. (A) Schematic representation of the model showing all membrane currents for the two mutually inhibitory cells of the half-centre oscillator (HCO). Inward currents include the slow calcium current (I_{CaS}), fast Na^+ current (I_{NaF}), persistent Na^+ current (I_{NaP}), Na^+ leak current ($I_{L\text{-}Na}$), and the hyperpolarization-activated cation current (I_h). Outward currents are the potassium leak ($I_{L\text{-}K}$), delayed rectifier potassium (I_{KDR}), A-type potassium current (I_{KA}), Na^+/K^+ pump current (I_{Pump}), and inhibitory synaptic current (I_{Syn}). (B) Membrane potential of 2 model cells which burst in alternation within an episode. The time course for membrane potential of each half of the HCO illustrates intra-episode activity (green; B), and state variables of the left neuron: (h_{NaP}; C) inactivation of persistent Na^+ current, ($[Na_i]$; D) intracellular Na^+ concentration , (E) I_{Pump}, and (m_h; F) activation of I_h, which slowly deactivates during the episode and promotes the episode's termination.

mature zebrafish (Currie et al., 2016; Gabriel et al., 2011; Müller et al., 2000).

Key parameters for producing episodic rhythmicity

We identified ranges of parameters around their canonical values (one at a time) within which our HCO model exhibited episodic activity. Changing I_{Pump}, I_h, and I_{NaP} can move the system into and out of a zone supporting episodic bursting. The intra-episode pattern was characterized by alternating bursting between HCO neurons. I_h is a mixed ion current carried by Na^+ and K^+ ions and it's activation (m_h) is the slowest variable of the system. Thus, in addition to its role as a predominantly inward current, I_h also contributes to intracellular Na^+ concentration ($[Na^+]_i$), which is the second slowest variable of the system. In each case of the specific parameter variation, we compared changes predicted by the model with experimental data from the isolated spinal cord preparation. We found that the cases of parameters of I_{Pump}, I_h, and the outward synaptic current (I_{Syn}) required careful adjustment to fit the temporal characteristics of experimental data (Figure 1). A burst generating mechanism of our model was based on the dynamics of activation and inactivation of I_{NaP}, which controlled initiation and termination of individual bursts. I_h contributed to episode characteristics by controlling episode duration (ED) along with the I_{Pump} activated by $[Na^+]_i$.

Model-generated episodic rhythmicity is consistent with spinal rhythms generated in vitro

Overall, we tuned maximal pump current ($I_{PumpMax}$) and maximal conductances ($\bar{g}$) for I_h ($\bar{g}_h$), and I_{NaP} ($\bar{g}_{NaP}$) of the model such that it exhibited episodic bursting activity with temporal characteristics similar to episodes generated by isolated spinal cords in response to 50 µM dopamine

(Figure 2A, B; and see Supplemental Figure 1 for detailed analysis of in vitro episodic bursting). Using the parameters maximal $I_{PumpMax}$ = 40 pA, $\bar{g}_h$ = 0.2645 nS, and, $\bar{g}_{NaP}$ = 5.0 nS, episodes generated by the model were not different from those recorded in vitro from the spinal cord (n = 8) in terms of EP (Figure 2D1, $t_{(33)}$= 0.9492, p = 0.3494 s), EP variability (EP-CV; Figure 2D2, $t_{(7)}$ = −0.2705, p = 0.7946) or episode duration (ED: $t_{(33)}$ = −2.0302, p = 0.0505; Figure 2D3). Furthermore, the model was capable of reproducing intra-episode burst period dynamics observed in vitro, with an intra-episode burst period that started short and increased in length during the episode (Figure 2C1, C2). Intra-episode bursting generated by the model, which started with a burst period of 0.1 s and increased to 1.0 s by the end of the episode differed compared to experimental data that started with a burst period of 0.65 ± 0.2 s, and increased to 0.9 ± 0.2 s.

Episodic rhythmicity depends on I_h

I_h plays an important role in a variety of rhythmic networks in both invertebrate (Angstadt and Calabrese, 1989; Peck et al., 2006) and vertebrate systems (Butt et al., 2002; Kjaerulff and Kiehn, 2001; Picton et al., 2018; Smith and Perrier, 2006; Takahashi, 1990; Thoby-Brisson and Ramirez, 2000) and dynamically interacts with I_{Pump} (Kueh et al., 2016; Picton et al., 2018; Tobin and Calabrese, 2005; Zhang et al., 2017). Leech heart single neuron and HCO studies demonstrated episodic bursting patterns at low $I_{PumpMax}$ strengths (Cymbalyuk, unpublished data). Consistent with those findings, we found I_h-dependent episodic bursting in both model-generated

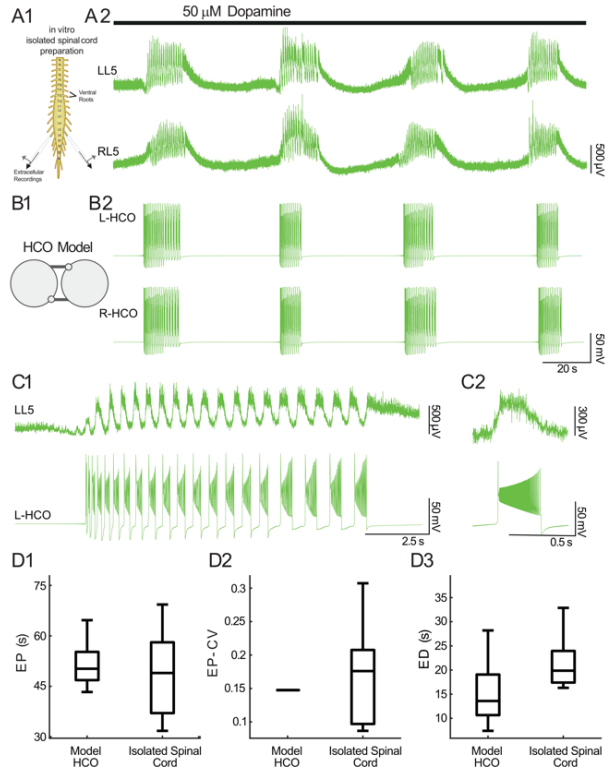

Figure 2: Temporal characteristics of dopamine-evoked episodic rhythmicity in the isolated spinal cord, reproduced by a biophysical model. (A1) Depicts in vitro preparation used to obtain extracellular neurograms from isolated spinal cords of newborn mice. (A2) Episodes of rhythmic activity generated by isolated spinal cords with dopamine (50 μM). Neurograms represent recordings from left and right L5 ventral roots. (B1) The half-centre oscillator (HCO) model was tuned to produce episodic rhythmicity (B2). (C1) Similar intra-episode rhythm features in a single episode of activity recorded experimentally (top trace) and from the model (lower trace) show bursting slowing down over the course of the episode. (C2) A single intraepisode burst recorded experimentally (top trace) corresponds to a single burst within the model (lower trace). (D1) Model-generated episodes (bottom trace) of activity match the recordings (top trace) in terms of episode period (EP; 50.2 s, p = 0.35), (D2) episode period variability (EP-CV; 0.15, p = 0.79), and (D3) episode duration (ED; 13.6 s, p = 0.05). Box and whisker plots depict interquartile range (boxes), median (horizontal black lines), maximum, and minimum values in data range (whiskers).

data and dopamine-elicited neurograms recorded in spinal cords in vitro.

Variation of $\bar{g}_h$ revealed four zones of parameter space that produced distinct activity patterns (silent, episodic bursting, continuous bursting, and tonic spiking; Figure 3). The model HCO was silent when $\bar{g}_h$ was below 0.2454 nS, exhibited stable episodic bursting (EP-CV = 0.05) when $\bar{g}_h$ ranged from 0.2454 to 0.2702 nS (Figure 3B1-B3), a continuous bursting when $\bar{g}_h$ was between 0.2699 and 8.205 nS, and transitioned to a tonic spiking activity when $\bar{g}_h$ was above 8.205 nS (not shown). We investigated changes in episode characteristics including the ED, inter-episode intervals, (IEI) the number of bursts per episode, and properties of individual fast bursts within episodes. Within the zone supporting episodic bursting, as $\bar{g}_h$ increased from 0.2454 to 0.2702 nS, ED increased from 9.5 to 16.7 s (Figure 3C1). At the onset of the episodic bursting, EP and IEI were 128.2 and 118.7 seconds, respectively, and decreased to 31.2 and 15.5 seconds, respectively, prior to the transition to continuous bursting (Figure 3C2). The EP-CV did not rise above 0.07; however, after the model transitioned to continuous bursting above 0.2702 nS, cycle period variability (cCP-CV) did not exceed 0.01 (Figure 3 C3: red dots). We also found a multistable zone where episodic and continuous bursting patterns coexisted when $\bar{g}_h$ was within a narrow range of intermediate values (0.2699 nS–0.2702 nS). Within this zone, the model generated either continuous or episodic rhythms, depending on the initial state of the HCO (Figure 3B5, B6). Because our model is deterministic and does not include noise in its dynamics, the set of the initial state variables (initial conditions) determines which rhythmic pattern out of the coexisting two is exhibited by the HCO.

Consistent with our model, in isolated spinal cord preparations (n = 11), blocking I_h channels with ZD7288 significantly impacted episodic bursting. The direction and magnitude of change in EPs corresponded to the predicted effects, whereas EDs trended in the opposite direction of that predicted by the model. In the presence of ZD7288, dopamine (50 µM) depolarized the ventral root neurogram (Figure 3D1), followed by the emergence of episodic rhythmic bursting (Figure 3D2). Compared to episodes elicited by preparations with dopamine alone (n = 8), dopamine-evoked episodes in the presence of ZD7288 had a shorter EPs ($t_{(16)} = 3.5$, $p = 0.003$, EP = 31.4 ± 7.9 s (mean ± SD); Figure 3E1), were more irregular (EP-CV Mann–Whitney $W = 14$, $p = 0.02$; Figure 3E2), shorter durations (Mann–Whitney $U = 14$, $p = 0.02$, ED = 15.9 ± 7.0 s (mean ± SD); Figure 3E3) and had smaller amplitudes ($t_{(16)} = 3.9$, $p = 0.001$; Figure 3E4).

Modulation of I_{Pump} leads to transitions between episodic and continuous bursting

In our model, we found that episodic bursting was dependent on I_{Pump} (Figure 4A). The model was silent when $I_{PumpMax}$ was below 16.85 pA, and when $I_{PumpMax}$ was above 16.85 pA, the model exhibited continuous bursting composed of irregular plateau-like bursts: an initial spike followed by a plateau potential (with no spiking) for

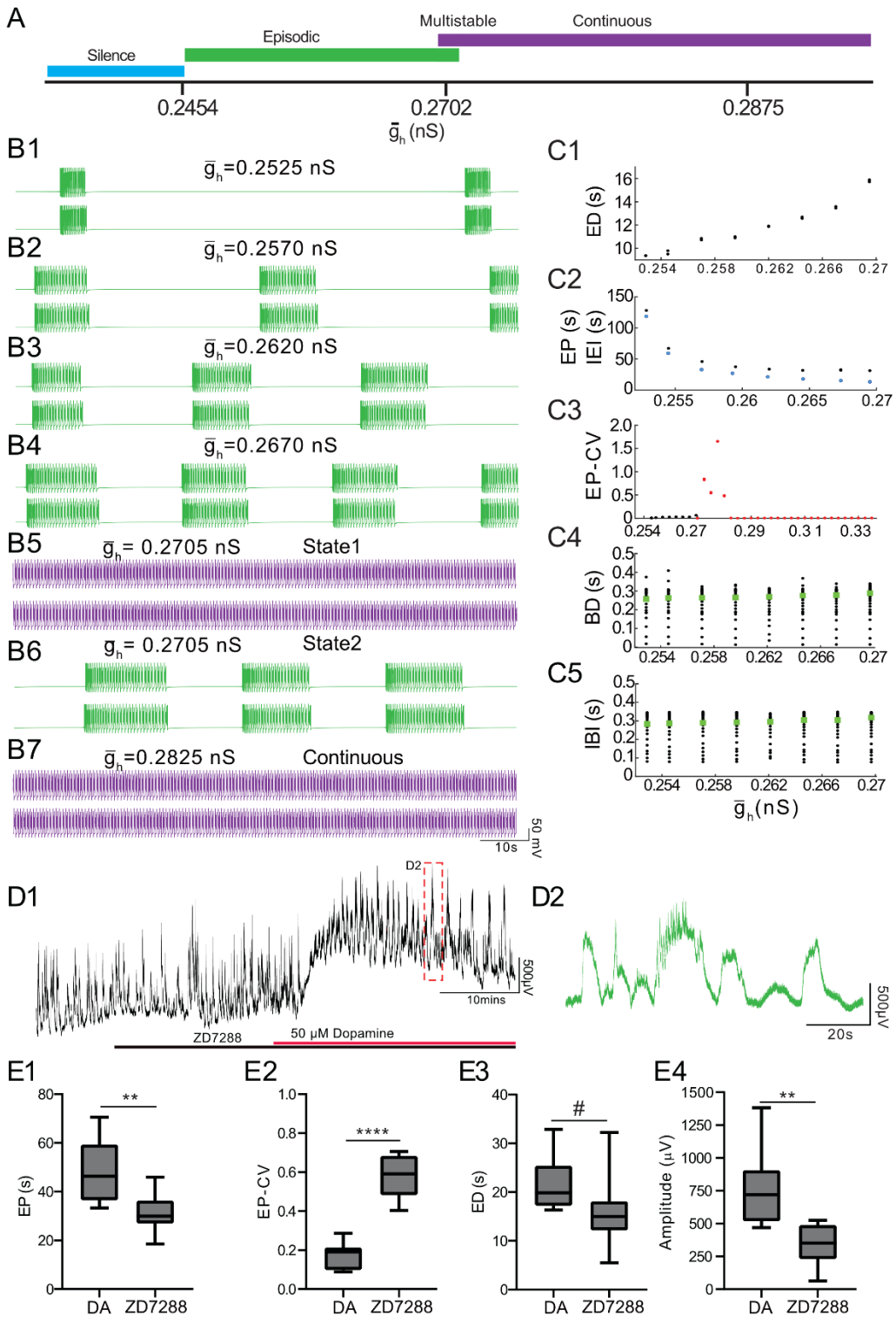

Figure 3: Regulation of $\bar{g}_h$ modified episodic bursting activity and led to transition to continuous bursting in the model, and I_h supported episodic rhythmicity in vitro. (A) Colour bar depicts the boundaries of each modelled activity (silence, blue; episodic, green; and continuous, purple). As $\bar{g}_h$ increased, the model output transitioned from silence to episodic bursting at 0.2454 nS, and then from episodic to continuous bursting at 0.2702 nS. The model exhibited continuous bursting above 0.2699 nS and coexistence of episodic and bursting patterns between the …

…latter two boundaries (B5, B6). (B) Small increases in the maximal conductance of I_h ($\bar{g}_h$) caused notable changes in the episodic bursting pattern (B1–B4, B7). (C) Episode duration (C1) increased by 59.27% and the episode period and inter-episode interval decreased dramatically by factors of 7.73 and 4.11, respectively (C2). (C3) The coefficient of variation for episode period (EP-CV, black) and continuous bursting period (cCP-CV, red). Variation of $\bar{g}_h$ did not alter the distribution (black dots) or average (green dots) intra-episode burst duration (BD: C4) or interburst interval (IBI: C5) (D) Extracellular neurograms (D1) recorded from a single ventral root show episodic rhythmicity evoked by dopamine (black bar) in the presence of the I_h channel blocker ZD7288 (30–50 μM, red bar). D2 expands the inset in D1. (E) ZD7288 reduced the episode period (EP; E1), increased episode period variability (EP-CV; E2), and reduced duration (ED; E3) and amplitude (E4) of episodes of dopamine-evoked rhythmicity. Box and whisker plots depict interquartile range (boxes), median (horizontal black lines), maximum, and minimum values in the data range (whiskers) for episodic rhythms evoked by dopamine alone (n = 8), or in the presence of ZD7288 (n = 11) in separate sets of experiments; asterisks indicate significance of unpaired t-tests (* $p < 0.05$; ** $p < 0.01$; *** $p < 0.001$; **** $p < 0.0001$); # indicate significance of non-parametric Mann-Whitney U test.

the first half of the burst, and smaller amplitude spiking for the rest of each burst duration (Figure 4B1). The model activity transitioned to continuous bursting at $I_{PumpMax}$ = 25.75 pA (Figure 4B2), to episodic bursting at $I_{PumpMax}$= 39.93 pA (Figure 4B3–5), and then again to continuous bursting at $I_{PumpMax}$= 90.05 pA (Figure 4B6). Thus, both a decrease and an increase in $I_{PumpMax}$ from the canonical value for episodic bursting ($I_{PumpMax}$= 40 pA) caused the HCO to transition from episodic bursting to continuous bursting. As $I_{PumpMax}$ increased within the range supporting episodic bursting, ED (Figure 4C1) and EP (Figure 4C2) increased exponentially, and IEIs decreased exponentially (Figure 4C2, blue). The rate of change for ED and EP became particularly prominent when $I_{PumpMax}$ increased to above 60 pA, where the Δ $I_{PumpMax}$ had a greater effect on ED, relative to its effect on IEI. At the lower boundary, between episodic activity and continuous activity (~ 40 pA), there was a slight decrease in ED and bursts per episode. When $I_{PumpMax}$ increased above 46 pA, both of these characteristics began to increase. Along with this trend, when $I_{PumpMax}$ was between 40 pA and 52 pA, the intra-episode distribution of burst duration and interburst intervals (IBI) changed; we observed a shift toward a more consistent distribution that collapsed as episodes increased in duration, before the pattern of activity transitioned into continuous rhythmic activity (Figure 4C4–5). Similar to $\bar{g}_h$, we also found a multistable zone where episodic and continuous bursting patterns coexisted when $I_{PumpMax}$ was within a range of intermediate values (39.93–40.00 pA).

We tested our model's predictions against the effect of manipulation of I_{Pump} on rhythmic activity in the isolated spinal cord preparation. The activity-dependent I_{Pump} is important for episodic rhythmic activity in biological systems (Pulver and Griffith, 2010; Zhang et al., 2015; Zhang and Sillar, 2012). It controls disinhibited rhythmicity in isolated rodent spinal cords (Ballerini et al., 1997) and it can be modulated by dopamine (Picton et al., 2017).

Specifically, we tested whether blocking the pump with different concentrations of ouabain affects dopamine-evoked rhythms. Ouabain has dose-dependent effects on the I_{Pump}, preferentially

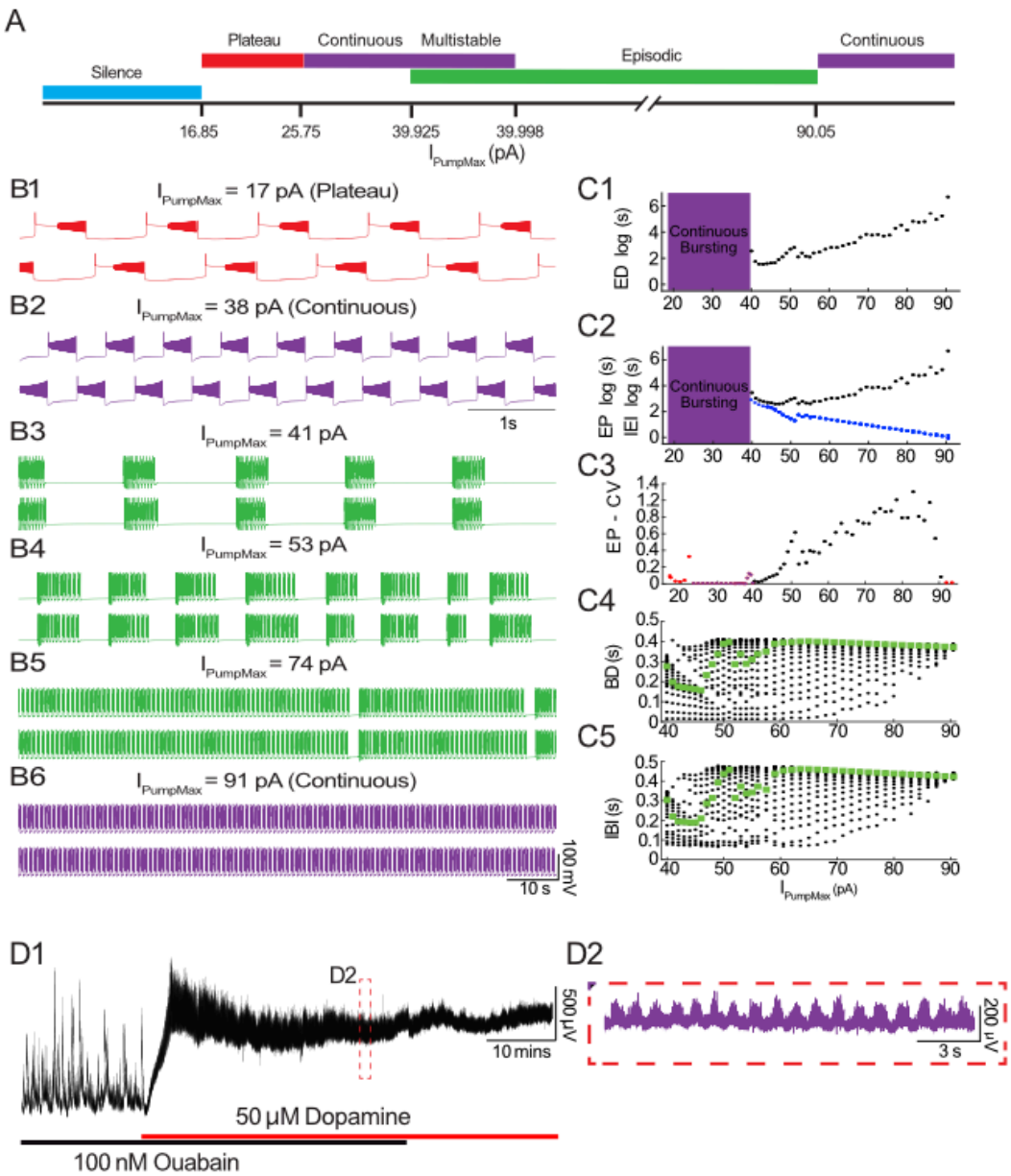

Figure 4: Variation in $I_{PumpMax}$ modulates episodic bursting properties and produces transitions between episodic and continuous rhythmicity. (A) The colour depicts boundaries of zones supporting each modelled pattern when $I_{PumpMax}$ was varied (silence, blue; plateau, red; episodic, green; continuous, purple). Two separate continuous bursting zones surround the zone supporting episodic bursting. The episodic bursting zone spanned a range of $I_{PumpMax}$ values from 39.93 to 90.05 pA. (B1) The model produced plateau bursting (red) for $I_{PumpMax}$ between 16.85 and 25.75 pA. (B) Relative to the canonical value of $I_{PumpMax}$ ($I_{PumpMax}$ = 40 pA), upregulation and downregulation caused transitions from episodic bursting activity (B3–B5) to continuous bursting activity (B2, B6). (C) Episode duration (ED; C1) and episode period (EP; C2, black) increased along with $I_{PumpMax}$, whereas inter-episode interval (IEI; C2, blue) decreased. EP and ED showed similar trends, although EP showed less change prior to 52 pA due to longer IEIs than EDs. These trends abruptly changed at 53 pA, after which ED and EP increased and, and IEI decreased exponentially, with log-transformed rates (s/pA) of 0.0947, 0.0829, and −0.0445, respectively. (C3) We calculated the episode period coefficient of variation for the entire span of both episodic (EP-CV, black) and continuous patterns (cCP-CV, purple); there was a small increase in cCP-CV at the edges of the continuous bursting …

… activity, between silence and episodic bursting. EP-CV increased as $I_{PumpMax}$ increased in the range of 40–82 pA and then fell prior to transitioning to the upper continuous bursting activity. Episode temporal characteristics, excluding EP-CV were log transformed because they spanned a wide range of values. Distributions (black dots) and mean (green dots) intraepisode burst durations (BD: C4) and interburst intervals (IBI: C5) depict progressive changes of bursting properties within episodes between 40 pA and 90.05 pA, where they shifted toward a more consistent distribution. This intra-episode structure collapses as episodes increase in duration and transition to continuous bursting activity. (D1) Extracellular neurogram recorded from ventral roots with bath application of 100 nM ouabain (red bar along x-axis) followed by 50 μM dopamine (black bar along x-axis) exhibits continuous rhythmic activity. The trace in D2 represents an expanded segment of the fast-continuous rhythmic activity outlined by the red dashed box in D1.

disrupting the alpha-3 subunit and dynamic pump function at low concentrations, and blocking the alpha-1 subunit at higher concentrations. Prior to application of dopamine, ouabain concentrations of 1 µM (n = 6; mean ± SD Δ DC potential = 3433 ± 1897 µV;) and 500 nM (n = 2; mean ± SD Δ DC potential = 738 ± 128 µV) dose-dependently depolarized ventral root DC potentials ($F_{(2,11)}$ = 9.7, p = 0.004; Supplemental Figure 3A1, B1;) and suppressed spontaneous network activity (Supplemental Figure 3B3: $F_{(2,11)}$ = 10.5, p = 0.003). Subsequent application of dopamine further depolarized the ventral roots but did not elicit any superimposed rhythmicity (Supplemental Figure 3A2), consistent with the silent state predicted by the model at the lowest $I_{PumpMax}$ strengths. As predicted by the model, reducing ouabain concentration to 100 nM produced dopamine-mediated continuous rhythmic bursting with burst metrics within a range as those generated by the model (Figure 4D1, D2). Continuous bursting elicited by dopamine in the presence of 100 nM of ouabain had a mean cycle period (CP) of 1.45 ± 0.37 s, a CP-CV of 0.22 ± 0.07, burst duration of 0.93 ± 0.33 s, IBI of 0.50 ± 0.2 s, and an amplitude of 298.4 ± 105.1 µV. Episodic bursting returned in three of six preparations following a wash with 50 µM dopamine in regular aCSF (not shown).

Persistent Na^+ current contributes to episodic bursting rhythmicity

Persistent Na^+ (I_{NaP}) and calcium (I_{CaL}) currents mediate endogenous bursting properties and contribute to the generation of rhythmic behaviours in a variety of systems (Brocard et al., 2013; Del Negro, 2005; Song et al., 2020; Tazerart et al., 2008; Zhong et al., 2007). In our model, I_{NaP} contributed to the initiation of bursts and supported the burst phase of individual fast bursts. The importance of $\bar{g}_{NaP}$ for producing rhythmic bursting was evidenced by the relatively high conductance required to produce rhythmic activity; the model output was silent below $\bar{g}_{NaP}$ = 4.985 nS (not shown). We observed episodic bursting within a narrow range of $\bar{g}_{NaP}$ (4.985–5.010 nS; Figure 5B1–B4). Continuous bursting occurred from a $\bar{g}_{NaP}$ of 5.010 to 6.850 nS (Figure 5B5), and changed to plateau bursting with a depolarization block after the first spike of the burst, and finally, slowly depolarized without spikes after 10 nS (not shown). As $\bar{g}_{NaP}$ increased within the narrow range that produced episodic bursting, ED increased from 11 s to 15 s (Figure 5C1), and EP and IEI decreased

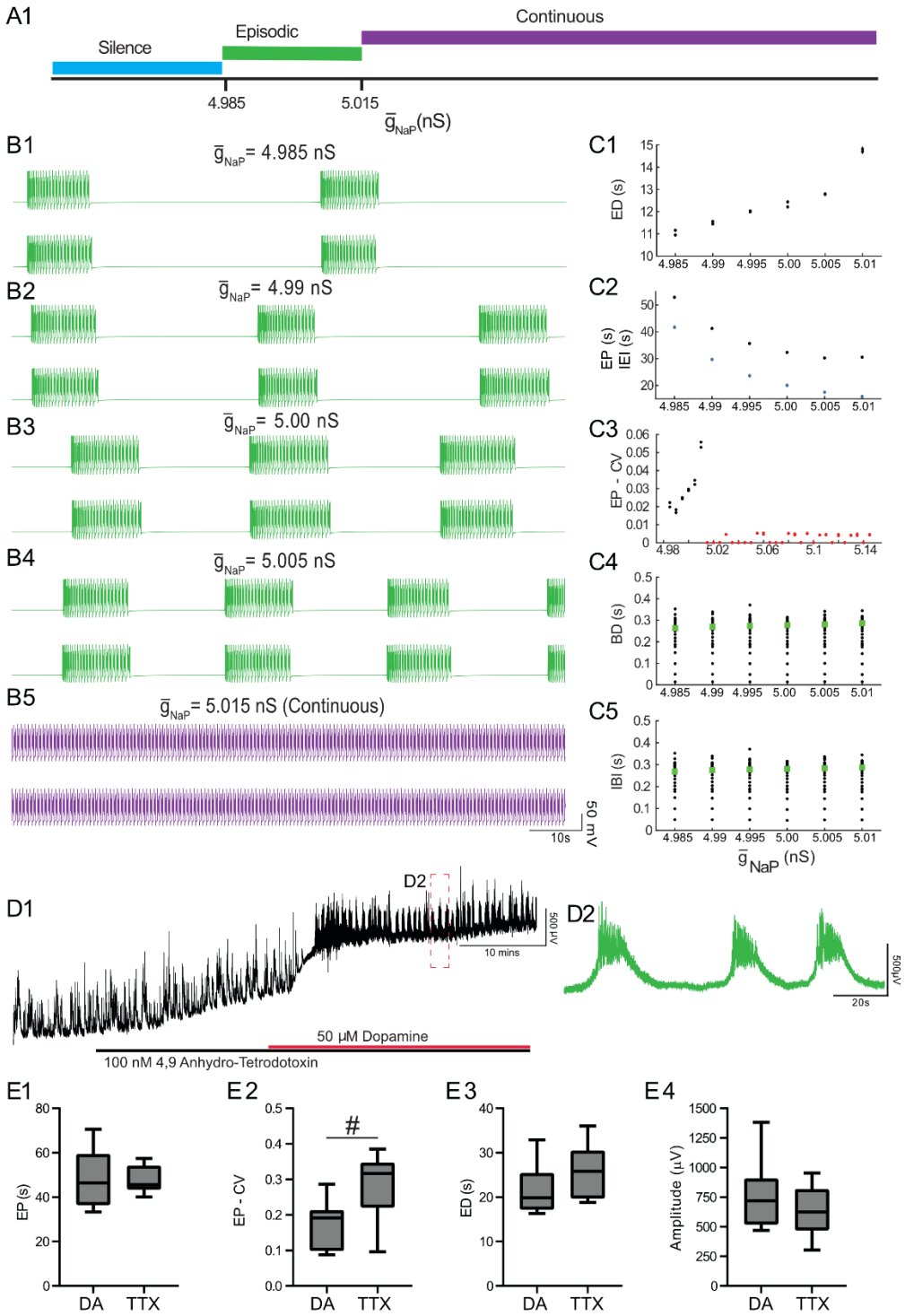

Figure 5: I_{NaP} strongly affects episodic bursting in the model and stabilizes episodic rhythmicity in vitro. (A) The colour bars show the boundaries of each modelled pattern when $\bar{g}_{NaP}$ varied (silence, blue; episodic, green; continuous, purple). (B) Half-centre oscillator (HCO) episodic bursting activity changed with small increases in $\bar{g}_{NaP}$ (B1-B4) and then transitioned to continuous bursting (B5). (C) Although increasing $\bar{g}_{NaP}$ increased episode duration (C1), episode period (C2: black dots) and inter-episode interval decreased (C2: blue dots). (C3) Episodic and continuous patterns were both robust, although the episode period's coefficient of variation (EP-CV) increased sharply from 2% to 6% (C3, black) before switching to continuous bursting activity (red). During the episodic …

… bursting, distribution (black dots) and average (green dots) intraepisode burst duration (BD: C4) and interburst intervals (IBI: C5) within episodes were unaffected by changes in $\bar{g}_{NaP}$ values. (D1) Extracellular neurograms show single ventral root episodic rhythmicity evoked by dopamine (50 µM; black bar) in the presence of the voltage-gated Na^+ ($Nav_{1.6}$) channel blocker 4,9 anhydro-tetrodotoxin (4,9 AH-TTX; 100–200 nM: red bar). D2 expands the inset in D1. Dopamine-evoked episode period variability (EP-CV) increased in the presence of 4,9, AH-TTX (D2), but episode period (E1), episode duration (E3), and episode amplitude (E4) did not change (unpaired *t*-tests). Box and whisker plots display interquartile range (boxes), median (horizontal black lines), maximum, and minimum values within the data range (whiskers) for episodic rhythms evoked by dopamine alone (n = 8) or in the presence of 4,9 AH-TTX (n = 11) in separate sets of experiments. # indicate significance ($p < 0.05$) of non-parametric Mann-Whitney U test.

from 53 s to 30.55 s and from 42 s to 15.8 s, respectively (Figure 5C2.). Of note, episodic bursting pattern remained relatively robust compared to when we manipulated $\bar{g}_h$, or $I_{PumpMax}$. EP-CV at the onset of episodic activity was 0.021, decreased to 0.0175, and increased to 0.06 before transitioning to continuous bursting. For continuous bursting, cCP-CV did not rise above 0.006. Variation of $\bar{g}_{NaP}$ did not alter BD (Figure 5C4) or IBI (Figure 5C5) within episodes throughout the episodic bursting pattern.

I_{NaP} is mediated by $NaV_{1.6}$, which can be blocked by 4,9 anhydro-tetrodotoxin (4,9 AH-TTX). In the presence of this blocker, dopamine still evoked a population depolarization (Figure 5D1) and episodic bursting (Figure 5D2). In line with the model, we found that dopamine-evoked episodic bursting was more irregular in the presence of 4,9 AH-TTX (100–200 nM, n = 11; Mann–Whitney on EP-CV, $W = 10$, $p = 0.02$; Figure 5E2) with no change in EP ($t_{(14)} = 0.2$, $p = 0.8$; Figure 5E1), ED ($t_{(14)} = 1.4$, $p = 0.2$; Figure 5E3) or amplitude ($t_{(14)} = 0.95$, $p = 0.4$; Figure 5E4; Tazerart et al., 2008). We also examined the contribution of L-type calcium channels, which produce I_{CaL} (X. Li et al., 2007; Marcantoni et al., 2020); however, nimodipine (n = 6; 15 µM), did not alter any parameters of dopamine-evoked episodes (EP, $t_{(12)} = 0.6$, $p = 0.5$; EP-CV, $t_{(12)} = 0.4$, $p = 0.7$; ED, $t_{(12)} = 1.6$, $p = 0.13$; amplitude, $t_{(12)} = 0.4$, $p = 0.7$; Supplemental Figure 4).

Brief perturbations induce switching between patterns within multistable zones

A common feature of multistable systems is the ability to rapidly switch between states. In many biological systems, these switches can be triggered by brief inputs, or perturbations, to the system (Briggman et al., 2005; Briggman and Kristan, 2008; Chopek et al., 2019). In our model, we observed multistable zones within a narrow range of $\bar{g}_h$ (0.2699 – 0.2702 nS) and $I_{PumpMax}$ (39.93–40.00 pA), which produced continuous or episodic bursting patterns depending on the initial conditions of the model. The multistable zone for $I_{PumpMax}$ occupied a wider range of current strengths than the zone for conductance values of $\bar{g}_h$. Therefore, we tested the ability of brief perturbations to trigger switches between patterns within the $I_{PumpMax}$-induced multistable zone.

Consistent with the notion that brief perturbations trigger pattern switches, we found that when circuit parameters were

tuned to the multistable zone delimited or defined by $I_{PumpMax}$ = 39.94 pA, introducing a hyperpolarizing current pulse ($\bar{g}_{pulse}$ = 35.50 nS, pulse duration = 6 s) into both cells switched the model output from a continuous to an episodic pattern (Figure 6C); a short depolarizing current pulse into one cell ($\bar{g}_{pulse}$ = 35.50 nS, pulse duration = 0.4 s) could trigger a switch from an episodic to a continuous pattern (Figure 6D). Specific pulse parameters were required to trigger a switch between patterns while operating in a multistable zone. A hyperpolarizing pulse applied to both cells for less than 6 s, during continuous bursting produced a prolonged interburst interval but did not trigger a switch to episodic bursting. Similarly, a brief depolarizing pulse applied during episodic bursting could not trigger a switch to continuous bursting but could reset the episodic rhythm. Applying similar perturbations during monostable episodic ($I_{PumpMax}$ = 40 pA) or continuous patterns ($I_{PumpMax}$ = 35 pA) could not induce a switch; however, these perturbations reset the respective rhythms (Figure 6E, F).

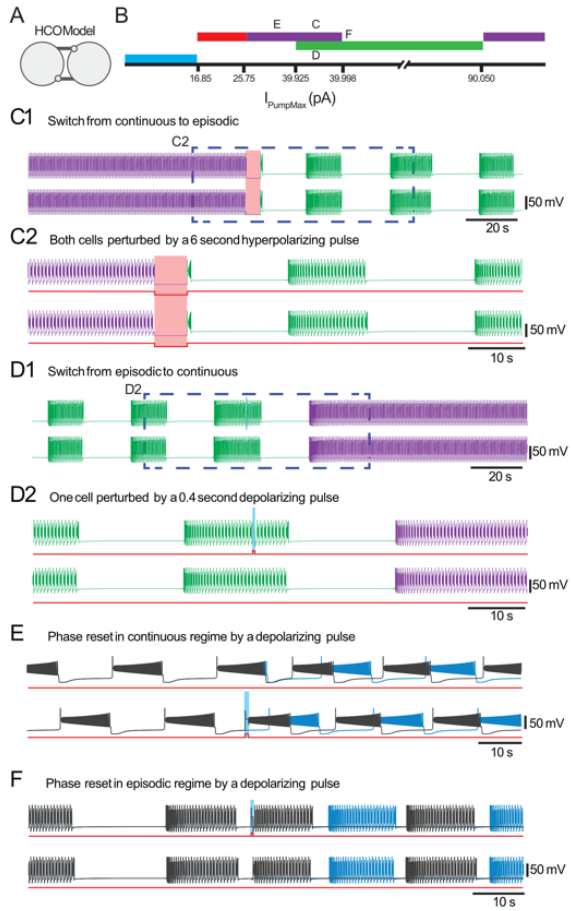

Figure 6: Specific perturbations trigger a switch between patterns in a multistable HCO and reset rhythms in a monostable HCO. (A) In the HCO model, when $I_{PumpMax}$ = 39.93 pA, the episodic and continuous bursting patterns coexisted, and brief perturbations caused rapid switches between patterns. The examples shown used a pulse of conductance that was either hyperpolarizing (red) or depolarizing (light blue), Red lines (C2, D2, E, F) represent current traces. (B) The model produced episodic or continuous patterns that were monostable or multistable depending on the value of $I_{PumpMax}$. Letters in B (C-E) depict the $I_{PumpMax}$ conditions under which we applied brief perturbations to the model. (C) Illustrates a switch from continuous (purple) to episodic bursting (green), elicited by a 6 s hyperpolarizing pulse of conductance (red box) delivered to both HCO cells. C2 expands the segment of data outlined by the dashed blue box in C1. (D) A switch from episodic to continuous bursting pattern triggered by a 0.4 s depolarizing pulse of conductance (light blue section) injected into one cell (top trace) …

Discussion

Spinal circuits produce a diverse array of rhythmic motor outputs, a subset of which can be generated at birth (Whelan et al., 2000). Episodic activity has been reported in developing spinal circuits for a range of species (Combes et al., 2004; Gozal et al., 2014; Marchetti and Nistri, 2001; McDearmid and Drapeau, 2006; Picton et al., 2018; Sharples and Whelan, 2017; Wiggin et al., 2012). We previously demonstrated that episodic and continuous patterns of rhythmic activity can be

… of the HCO. D2 expands the segment of data outlined by the dashed blue box in D1. Continuous (E) and episodic (F) bursting during an epoch with (blue traces) and without (black traces) stimulation. Continuous and episodic rhythms were reset by a 0.4 second depolarizing pulse of conductance (light blue section) injected into one cell when the HCO was operating in monostable regions of parameter space with $I_{PumpMax}$ = 40 for continuous (E), and 35 pA for episodic (F) patterns.

generated in vitro in perinatal mouse spinal cord. Transitions between patterns can be induced by manipulating neuromodulatory tone or excitability (Sharples and Whelan, 2017). Here, we focused on the cellular mechanisms that produce episodic and continuous patterns of rhythmic activity and the mechanisms that govern transitions between them. We developed a biophysical model that produces episodic and continuous patterns of bursting activity (Barbieri and Nistri, 2001; Gozal et al., 2014; Marchetti and Nistri, 2001; Sharples and Whelan, 2017) and investigated how key network and cellular properties contribute to their generation in isolated spinal cords. The model was a single CPG composed of two inhibitory half centres, with I_{Pump}, I_h, and I_{NaP} currents. We derived these parameters from insights based on studies on the dynamic roles of the I_{Pump} in the regulation of the leech heartbeat (Kueh et al., 2016; Tobin and Calabrese, 2005) and *Xenopus* tadpole locomotor CPGs (Picton et al., 2018; Zhang et al., 2015; Zhang and Sillar, 2012).

Our model produced episodic and continuous patterns of rhythmicity consistent with those elicited in vitro (Figure 2). Increasing the model's maximal conductances for I_h or I_{NaP} led to transitions from silent state to episodic bursting, and then to continuous bursting. Consistent with this finding, blocking these conductances pharmacologically destabilized episodic bursting evoked by dopamine in vitro (Figures 3, 5). The model revealed that either up or down regulation of $I_{PumpMax}$ produced a transition to continuous bursting, a finding supported by our in vitro pharmacological experiments (Figure 4). Our results demonstrate that multiple pathways can lead to transitions between episodic and continuous rhythmic patterns (Figure 7). This finding is consistent with studies modelling the stomatogastric ganglion (STG), which demonstrated that disparate circuit properties produced similar outputs (Prinz et al., 2004) and led to transitions between circuit outputs (Gutierrez et al., 2013; Gutierrez and Marder, 2014). In addition to discrete regions of parameter space where our model exhibited only one type of activity (episodic or continuous), we found multistable zones where, depending on its initial state, the model produced both patterns having the same set of parameters. In these multistable zones, perturbations triggered rapid switching between episodic bursting and continuous bursting. Outside the multistable zones, brief perturbations reset episodes during episodic bursting activity or individual bursts during continuous bursting activity, indicating state-dependent control of inputs to the CPG. This is noteworthy because isolated perinatal spinal cord produces a rich repertoire of activity patterns (Whelan et al., 2000), and although in many spinal circuits, diverse

outputs are supported by recruitment of circuit elements (Ampatzis et al., 2014; Bellardita and Kiehn, 2015; Calabrese and Wright, 2014; Crone et al., 2009; Dougherty and Kiehn, 2010), our work suggests that a single multifunctional CPG can generate at least a subset of these patterns.

Dynamic mechanisms lead to transitions between episodic and continuous rhythmic activity in a single developing CPG

We provide an analysis of cellular dynamics when each element in our model is individually manipulated, and we find parallel changes in biological network behaviour when these elements are individually blocked pharmacologically. Critically, some of the currents we studied here, such as I_{NaP}, are present in spinal neurons as early as embryonic day (E) 12 (Boeri et al., 2018; Kuo et al., 2006), suggesting that modulating conductances within a simple circuit can produce diverse output patterns. Similarly, I_h may contribute to circuit development in rodents (Yang et al., 2018), and is present in rat cultured motoneurons from E14 (Elliott et al., 1999). The pump-mediated ultraslow afterhyperpolarization (usAHP) is also expressed in mouse spinal inter- and motoneurons at early postnatal stages, and is modulated by dopamine (Picton et al., 2017). Of the properties established in our model, we found that I_{Pump} plays a critical role in generating episodic bursting. In line with our model, blocking the pump with low concentrations of ouabain (100 nM), which selects toward blocking the alpha-3 subunit of the pump, promotes transition to continuous bursting. In contrast, higher concentrations of ouabain (0.5–1 μM) inhibited rhythmic activity in the presence of dopamine. Interestingly, increasing $I_{PumpMax}$ in the model also prompted a transition from episodic to continuous bursting. Increased pump activity may produce transitions from episodic to continuous locomotor behaviours observed during development in fish and tadpoles (Buss and Drapeau, 2001; Gabriel et al., 2011; Hachoumi and Sillar, 2020; Lambert et al., 2012; Müller et al., 2000). However, our work raises the possibility that a reduction in dynamic pump function may also generate such transitions. Thus, modulating the pump's function may change the mode of operation during development (Gonzalez-Islas et al., 2020), in addition to dynamically regulating locomotor behaviour.

The I_{Pump} supports homeostatic and dynamic functions based on the varying sensitivities of the alpha-1 and alpha-3 subunits to intracellular Na^+ concentrations. On the single-cell level, dynamic pump action is linked to the alpha-3 subunit and leads to an usAHP following the intense firing of action potentials (Picton et al., 2018, 2017; Pulver and Griffith, 2010; Tiwari et al., 2018; Zhang et al., 2015; Zhang and Sillar, 2012). In the spinal cord, the usAHP of the membrane potential determines future activity based on past neuronal activity, creating short term motor memory (STMM; Picton et al., 2017; Zhang et al., 2015; Zhang and Sillar, 2012). Our model indicates that episodic activity is generated across a range of $I_{PumpMax}$ strengths. We did not examine

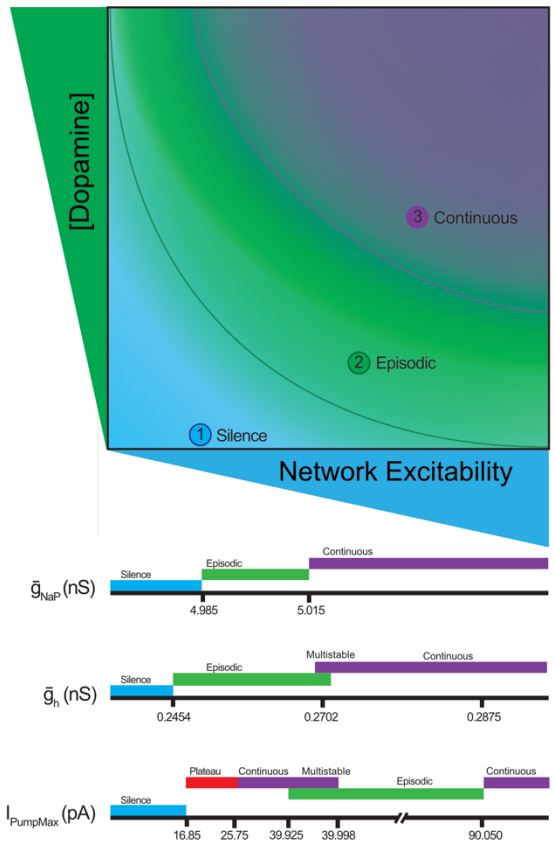

Figure 7: Neuromodulators evoke diverse rhythmic outputs by moving the network through an excitation-based parameter space by altering $I_{PumpMax}$, $\bar{g}_h$, and $\bar{g}_{NaP}$. State-dependent network activity, characterized by silence (blue), episodic (green), and continuous (purple) bursting patterns, generated by a central pattern generator under varying neuromodulatory tone (eg. dopamine) or excitability can be produced by varying $\bar{g}_{NaP}$, $\bar{g}_h$, $I_{PumpMax}$. Multistable zones (green-purple overlap) occurred at transitions between episodic and continuous bursting patterns within narrow ranges of $\bar{g}_h$ and $I_{PumpMax}$, where rapid switches were triggered by brief, but specific perturbations.

STMM within the episodic bursting, but an interesting possibility is that modulating maximal pump strength during episodic activity may lead to varying degrees of STMM. This suggests that STMM may not only be subject to neuromodulation, but may also be state-dependent.

The dynamic function of the pump is sensitive to fluctuations in intracellular Na^+ concentration, which is driven by Na^+ conductances that often endow interneurons with intrinsic properties to support rhythmic bursting. For example, I_{NaP} has been implicated as a key conductance for generating rhythmic oscillations in neurons (Butera et al., 1999; Del Negro et al., 2002; Jasinski et al., 2013; Koizumi and Smith, 2008; Tazerart et al., 2007; Zhong et al., 2007). In our model, a relatively high conductance was needed to produce episodic activity, which was observed within a relatively narrow range of conductance, prior to transitioning to continuous bursting.

Rhythm-generating interneurons also often express the mixed cation-conducting I_h (Borowska et al., 2013; Dougherty and Kiehn, 2010; Wilson et al., 2005), which is activated at hyperpolarized potentials and supports release from inhibition, which in turn facilitates burst initiation. Similarly, in the *Xenopus* tadpole spinal cord CPG, I_h is expressed only in glutamatergic rhythm-generating interneurons (dINs), where it opposes and cancels out the inhibitory I_{Pump}. Further, blockade of I_h disrupts STMM (Picton et al., 2018), suggesting that a balance between I_{Pump} and I_h is required for STMM. I_{Pump} also interacts with I_h in leech heartbeat neurons, which accounts for the paradoxical speeding up of the rhythm when I_{Pump} is increased experimentally with monensin (Kueh et al., 2016). Similarly, reducing $I_{PumpMax}$ can also produce episodic activity in a HCO model of leech heart interneurons (Cymbalyuk, unpublished data). Our data is consistent with this; we

found that increasing both $I_{PumpMax}$ and I_h led to a transition from episodic to continuous rhythms. Taken together, our data support the idea that multiple mechanisms can lead to transitions between episodic and continuous bursting patterns and extends the pump's diverse functions in the dynamic regulation of neuronal excitability described in a wide range of model systems (Ballerini et al., 1997; Gerkau et al., 2019; Kueh et al., 2016; Picton et al., 2018; Tiwari et al., 2018; Zhang and Sillar, 2012; Zhang et al., 2017).

Multistable zones facilitate rapid transitions between patterns

Rhythmically active circuits need to be robust enough to maintain output, yet flexible enough to rapidly adapt to changing demands. STG-inspired modelling studies have elegantly highlighted the fact that stable outputs within parameter space can be generated, with transitions facilitated by tuning circuit parameters (Gutierrez et al., 2013; Gutierrez and Marder, 2013). Our experimental and modelling data support this notion. One possible mechanism is neuromodulation (Gutierrez and Marder, 2014; Marder et al., 2014). However, speed-dependent transitions between locomotor gaits occur instantaneously (Bellardita and Kiehn, 2015) and neuromodulators often act on a slower time course through intracellular G protein-coupled receptor signalling pathways. Therefore, gradual changes in circuit properties through these means cannot facilitate rapid transitions between states. Alternatively, transitions between gaits may be mediated by recruitment of new circuit elements (Bellardita and Kiehn, 2015; Crone et al., 2009). Our data suggest that an individual circuit element may also produce rapid switching between output modes.

While manipulating $\bar{g}_h$ or $I_{PumpMax}$ in our model, we found multistable zones of parameter space in which identical sets of parameters produced either episodic or continuous bursting patterns. In computational biophysical models of single cells and neural networks, multistability is a common feature (Barnett et al., 2013; Bose et al., 2001; Goldbeter, 2018; Malashchenko et al., 2009; Marin et al., 2011; Parker et al., 2018), but it is less commonly reported in biological networks (Mackie and Meech, 1985). Multistability is a regularly reported phenomenon on the single cell level (Guttman et al., 1980; Turrigiano et al., 1996) that underlies up and down states of excitability in individual neurons across the CNS (Chopek et al., 2019). Multistable properties of spinal motoneurons and interneurons are mediated by Na^+ and calcium-dependent persistent inward currents and K^+ currents (Bos et al., 2018) and serve a wide range of motor control functions (Brocard et al., 2013; Chopek et al., 2019; Lee and Heckman, 1998). Although the multistable zone generated by our model occurred within a narrow range for two of our parameters, we propose that coexistence of these patterns in a biological system may be promoted and expanded by neuromodulatory drive. In computational models, applying the theory of dynamical systems will support investigations of neuromodulation-induced changes that widen the multistable zone of parameter space (Bose et al., 2001; Goldbeter, 2018;

Malashchenko et al., 2009; Marin et al., 2011; Parker et al., 2018).

Multistable zones of parameter space provide an additional mechanism for pattern switching and affords a more rapid timescale. Within multistable zones, brief inputs can trigger transitions between episodic and continuous patterns (Barnett et al., 2013; Bondy et al., 2016; Malashchenko et al., 2011; Parker et al., 2019). For the spinal locomotor CPG, these switches could arise from synaptic input from sensory afferents or descending inputs. Therefore, we propose that neuromodulators alter circuit properties to position the network within regions of state-space that would favour stable outputs or, in the case of multistable zones, facilitate rapid transitions between states. This is consistent with work demonstrating that serotonin can elicit swimming (Kristan and Nusbaum, 1982; Willard, 1981) and dopamine can elicit crawling in leech (Crisp et al., 2012; Puhl and Mesce, 2008). Rapid transitions between swimming and crawling can be facilitated by sensory stimulation, which can be biased through hyperpolarization or depolarization of a single neuron in the circuit (Briggman et al., 2005). In line with this, stimulation of the pina in cortex-ablated cats can elicit either fictive scratch or fictive locomotion, with a bias toward locomotion when serotonin or glutamic acid is applied to the spinal cord (Duenas-Jimenez et al., 2017). These examples of rapid switching may be facilitated by networks operating within a multistable zone of parameter space.

Caveats, limitations, future directions, and new questions

Here we present the first example of a model CPG that produced episodic and continuous patterns of rhythmic activity; albeit, the model generated the episodic pattern within only a narrow range of the parameters we explored. Episodic rhythmicity generated by the isolated spinal cord is remarkably robust and can persist for hours in vitro. While our model was composed of two reciprocally connected cells with single compartments, we expect the episodic activity to be more robust with the integration of multiple compartments, or with an increase in number of cells that form a network, in combination with neuromodulation. Future investigations will explore factors that mediate robustness of the episodic rhythmicity.

Our results demonstrate the capacity of a single CPG to produce multiple rhythmic patterns by modulating circuit properties. Recruitment of neural ensembles or modules may also generate different patterns of rhythmic activity. Orderly recruitment of discrete motor modules in the zebrafish permit speed control (Gabriel et al., 2011; Jha and Thirumalai, 2020; McLean et al., 2007; Song et al., 2020). The emergence of more complex locomotor behaviours during development coincides with the integration of newly born populations of hindbrain V2a interneurons with intrinsic properties and modular synaptic connectivity to accommodate specific locomotor behaviours (Pujala and Koyama, 2019). Similarly, qualitatively different motor behaviours can be generated through the

recruitment of "specialist" neuronal populations; however, many behaviours share 'generalist' populations (Liao and Fetcho, 2008). One possibility is that these shared populations of neurons that engage during multiple motor behaviours act as nodes with tunable properties that afford switching between circuits (Gutierrez et al., 2013; Liao and Fetcho, 2008).

Our model indicates that an inhibitory circuit endowed with I_{Pump}, I_h, and I_{NaP} can produce episodic and continuous patterns. However, many rhythmic activities generated by the spinal cord are glutamate-dependent (Buchanan and Grillner, 1987; Dale and Roberts, 1984; Talpalar and Kiehn, 2010). Episodic swimming in larval zebrafish is generated by a distributed population of glutamatergic spinal neurons (Wiggin et al., 2014, 2012) and episodic rhythms elicited in isolated rat spinal cords are blocked by glutamatergic transmission blockers (Marchetti and Nistri, 2001). In support of those findings, our previous work demonstrated a role for NMDA receptors in maintaining episodic rhythms and enabling transitions to continuous rhythms (Sharples and Whelan, 2017). Recent work in the rodent hippocampus indicated that Na^+ pump subunits may directly interact with NMDA receptor complexes, providing a mechanism for ouabain-dependent modulation of NMDA conductances (Akkuratov et al., 2020). The Na^+ pump has been similarly implicated in regulating disinhibited rhythmicity in the neonatal rat spinal cord (Marchetti and Nistri, 2001). Future work adapting our model to include mutually excitatory synapses will shed light on this issue. Harnessing genetic tools available to study mice will also offer insight into putative "episode-generating" spinal interneurons. V3 interneurons are one population of interest, given their intrinsic (Borowska et al., 2013) and synaptic (Chopek et al., 2018; Danner et al., 2019; Zhang et al., 2008) properties, and their role in supporting locomotor bouts (Zhang et al., 2008). Alternatively, these functions may be supported by astrocytes that have broad, distributed connectivity, regulate locomotor-like activity in vitro (Broadhead and Miles, 2020), have well-established roles in regulating glutamatergic transmission at tripartite synapses, and extracellular K^+ homeostasis via Kir4.1 channels and I_{Pump} (Wang et al., 2012; Wotton et al., 2020).

Conclusion

Our modelling and in vitro experiments reveal that a single CPG produces multiple patterns of rhythmic activity and that degenerate mechanisms lead to transitions through modulation of I_{Pump}, I_h, or I_{NaP}. Some transitions are accompanied by multistable zones of parameter space, where brief, but specific perturbations induce rapid switching between patterns. In the context of locomotion, descending or sensory afferents could rapidly trigger pattern switching when the network is operating within a multistable zone. While episodic and continuous patterns have been well documented in isolated developing spinal circuits (Barbieri and Nistri, 2001; Gozal et al., 2014; Marchetti and Nistri, 2001; Sharples and Whelan, 2017), these activities may not be restricted to developing nervous systems;

there are many examples of these different patterns occurring in adult animals (Crawley, 2007; Gabriel et al., 2011; Müller et al., 2000; Wiltschko et al., 2015). This study provides insight into the network mechanisms that govern the generation of context-dependent locomotor patterns produced during different states in freely behaving animals and in developing motor networks.

Acknowledgements: We acknowledge support from the Whelan Lab. Spinal Core software was a kind gift from Prof A. Lev-Tov. We also thank Dr. Frederic Brocard for advice on the pharmacological blockade of $NaV_{1.6}$, and Tuan Bui, Ronald Calabrese, and Keith Sillar for helpful comments on an early version of the manuscript.

Funding: We acknowledge studentships from the Natural Sciences and Engineering Research Council of Canada (NSERC-PGS-D: SAS); Alberta Innovates (AIHS: SAS, APL); Hotchkiss Brain Institute (SAS, APL); and the Faculty of Veterinary Medicine (L.Y.). This research was supported by grants from the Canadian Institute of Health Research (PJW); an NSERC Discovery grant (PJW); National Institutes of Health, National Institute of Neurological Disorders and Stroke 1 R21 NS111355 (GSC and Ronald L. Calabrese).

Contributions: SAS, APL, and AS performed in vitro experiments and SAS analyzed the data with code written by LY. The computational model was developed and analyzed by AV, and GSC. SAS, AV, GSC, and PJW prepared figures and wrote the manuscript. All authors approved the final version of the manuscript. SAS, GSC, and PJW conceived and designed the research.

References

Akkuratov EE, Westin L, Vazquez-Juarez E, de Marothy M, Melnikova AK, Blom H, Lindskog M, Brismar H, Aperia A. 2020. Ouabain Modulates the Functional Interaction Between Na,K-ATPase and NMDA Receptor. *Mol Neurobiol*. doi:10.1007/s12035-020-01984-5

Ampatzis K, Song J, Ausborn J, El Manira A. 2014. Separate microcircuit modules of distinct v2a interneurons and motoneurons control the speed of locomotion. *Neuron* **83**:934–943.

Angstadt JD, Calabrese RL. 1989. A hyperpolarization-activated inward current in heart interneurons of the medicinal leech. *J Neurosci* **9**:2846–2857.

Arshavsky YuI, Beloozerova IN, Orlovsky GN, Panchin YuV, Pavlova GA. 1985. Control of locomotion in marine mollusc Clione limacina. IV. Role of type 12 interneurons. *Exp Brain Res* **58**:285–293.

Arshavsky YuI, Orlovsky GN, Panchin YuV, Pavlova GA. 1989. Control of locomotion in marine mollusc Clione limacina. VII Reexamination of type 12 interneurons. *Exp Brain Res* **78**:398–406.

Ballerini L, Bracci E, Nistri A. 1997. Pharmacological block of the electrogenic sodium pump disrupts rhythmic bursting induced by strychnine and bicuculline in the neonatal rat spinal cord. *J Neurophysiol* **77**:17–23.

Barbieri M, Nistri A. 2001. Depression of Windup of Spinal Neurons in the Neonatal Rat Spinal Cord In Vitro by an NK3 Tachykinin Receptor Antagonist. *J Neurophysiol* **85**:1502–1511.

Barnett W, O'Brien G, Cymbalyuk G. 2013. Bistability of silence and seizure-like bursting. *J Neurosci Methods* **220**:179–189.

Bellardita C, Kiehn O. 2015. Phenotypic characterization of speed-associated gait changes in mice reveals modular organization of locomotor networks. *Curr Biol* **25**:1426–1436.

Berg EM, Björnfors ER, Pallucchi I, Picton LD, El Manira A. 2018. Principles Governing Locomotion in Vertebrates: Lessons From Zebrafish. *Front Neural Circuits* **12**:73.

Berkinblit MB, Deliagina TG, Feldman AG, Gelfand IM, Orlovsky GN. 1978. Generation of scratching. II. Nonregular regimes of generation. *J Neurophysiol* **41**:1058–1069.

Berkowitz A. 2010. Multifunctional and specialized spinal interneurons for turtle limb movements. *Ann N Y Acad Sci* **1198**:119–132.

Boeri J, Le Corronc H, Lejeune F-X, Le Bras B, Mouffle C, Angelim MKSC, Mangin J-M, Branchereau P, Legendre P, Czarnecki A. 2018. Persistent Sodium Current Drives Excitability of Immature Renshaw Cells in Early Embryonic Spinal Networks. *J Neurosci* **38**:7667–7682.

Bondy B, Klishko AN, Edwards DH, Prilutsky BI, Cymbalyuk G. 2016. Control of Cat Walking and Paw-Shake by a Multifunctional Central Pattern Generator In: Prilutsky BI, Edwards DH, editors. Neuromechanical Modeling of Posture and Locomotion. New York, NY: Springer New York. pp. 333–359.

Borla MA, Palecek B, Budick S, O'Malley DM. 2002. Prey capture by larval zebrafish: evidence for fine axial motor control. *Brain Behav Evol* **60**:207–229.

Borowska J, Jones CT, Zhang H, Blacklaws J, Goulding M, Zhang Y. 2013. Functional subpopulations of V3 interneurons in the mature mouse spinal cord. *J Neurosci* **33**:18553–18565.

Bose A, Manor Y, Nadim F. 2001. Bistable Oscillations Arising from Synaptic Depression. *SIAM Journal on Applied Mathematics*. doi:10.1137/s0036139900378050.

Briggman KL, Abarbanel HDI, Kristan WB Jr. 2005. Optical imaging of neuronal populations during decision-making. *Science* **307**:896–901.

Briggman KL, Kristan WB. 2008. Multifunctional Pattern-Generating Circuits. *Annu Rev Neurosci* **31**:271–294.

Briggman KL, Kristan WB. 2006. Imaging Dedicated and Multifunctional Neural Circuits Generating Distinct Behaviors. *Journal of Neuroscience* **26**:10925–10933.

Broadhead MJ, Miles GB. 2020. Bi-Directional Communication Between Neurons and Astrocytes Modulates Spinal Motor Circuits. *Front Cell Neurosci* **14**:30.

Brocard F, Shevtsova NA, Bouhadfane M, Tazerart S, Heinemann U, Rybak IA, Vinay L. 2013. Activity-dependent changes in extracellular Ca2+ and K+ reveal pacemakers in the spinal locomotor-related network. *Neuron* **77**:1047–1054.

Buchanan JT, Grillner S. 1987. Newly identified "glutamate interneurons" and their role in locomotion in the lamprey spinal cord. *Science* **236**:312–314.

Buss RR, Drapeau P. 2001. Synaptic drive to motoneurons during fictive swimming in the developing zebrafish. *J Neurophysiol* **86**:197–210.

Butera RJ Jr, Rinzel J, Smith JC. 1999. Models of respiratory rhythm generation in the pre-Bötzinger complex. I. Bursting pacemaker neurons. *J Neurophysiol* **82**:382–397.

Butt SJB, Harris-Warrick RM, Kiehn O. 2002. Firing properties of identified interneuron populations in the mammalian hindlimb central pattern generator. *J Neurosci* **22**:9961–9971.

Calabrese R, Wright M. 2014. Faculty Opinions recommendation of Separate microcircuit modules of distinct v2a interneurons and motoneurons control the speed of locomotion. *Faculty Opinions – Post-Publication Peer Review of the Biomedical Literature*. doi:10.3410/f.718533516.793500088

Chopek JW, Hultborn H, Brownstone RM. 2019. Multistable properties of human subthalamic nucleus neurons in Parkinson's disease. *Proc Natl Acad Sci U S A* **116**:24326–24333.

Chopek JW, Nascimento F, Beato M, Brownstone RM, Zhang Y. 2018. Sub-populations of Spinal V3 Interneurons Form Focal Modules of Layered Pre-motor Microcircuits. *Cell Rep* **25**:146–156.e3.

Clemens S, Belin-Rauscent A, Simmers J, Combes D. 2012. Opposing modulatory effects of D1- and D2-like receptor activation on a spinal central pattern generator. *J Neurophysiol* **107**:2250–2259.

Combes D, Merrywest SD, Simmers J, Sillar KT. 2004. Developmental segregation of spinal networks driving axial- and hindlimb-based locomotion in metamorphosing Xenopus laevis. *J Physiol* **559**:17–24.

Crawley JN. 2007. What's Wrong With My Mouse? doi:10.1002/0470119055.

Cressman JR Jr, Ullah G, Ziburkus J, Schiff SJ, Barreto E. 2009. The influence of sodium and potassium dynamics on excitability, seizures, and the stability of persistent states: I. Single neuron dynamics. *J Comput Neurosci* **26**:159–170.

Crisp KM, Gallagher BR, Mesce KA. 2012. Mechanisms contributing to the dopamine induction of crawl-like bursting in leech motoneurons. *J Exp Biol* **215**:3028–3036.

Crone SA, Zhong G, Harris-Warrick R, Sharma K. 2009. In Mice Lacking V2a Interneurons, Gait Depends on Speed of Locomotion. *Journal of Neuroscience*. doi:10.1523/jneurosci.1206-09.2009

Currie SP, Combes D, Scott NW, Simmers J, Sillar KT. 2016. A behaviorally related developmental switch in nitrergic modulation of locomotor rhythmogenesis in larval Xenopus tadpoles. *J Neurophysiol* **115**:1446–1457.

Dale N, Roberts A. 1984. Excitatory amino acid receptors in Xenopus embryo spinal cord and their role in the activation of swimming. *The Journal of Physiology*. doi:10.1113/jphysiol.1984.sp015123

Danner SM, Zhang H, Shevtsova NA, Borowska-Fielding J, Deska-Gauthier D, Rybak IA, Zhang Y. 2019. Spinal V3 Interneurons and Left-Right Coordination in Mammalian Locomotion. *Front Cell Neurosci* **13**:516.

Del Negro CA. 2005. Sodium and Calcium Current-Mediated Pacemaker Neurons and Respiratory Rhythm Generation. *Journal of Neuroscience* **25**:446–453.

Del Negro CA, Koshiya N, Butera RJ Jr, Smith JC. 2002. Persistent sodium current, membrane properties and bursting behavior of pre-bötzinger complex inspiratory neurons in vitro. *J Neurophysiol* **88**:2242–2250.

Dougherty KJ, Kiehn O. 2010. Functional organization of V2a-related locomotor circuits in the rodent spinal cord. *Annals of the New York Academy of Sciences*. doi:10.1111/j.1749-6632.2010.05502.x

Dougherty KJ, Kiehn O. 2010. Firing and Cellular Properties of V2a Interneurons in the Rodent Spinal Cord. *Journal of Neuroscience*. doi:10.1523/jneurosci.4821-09.2010

Duenas-Jimenez SH, Hernandez LC, de la Torre Valdovinos B, Ruiz GM, Duenas Jimenez JM, Abundis VR, Garcia IGA. 2017. Hind limb motoneurons activity during fictive locomotion or scratching induced by pinna stimulation, serotonin, or glutamic acid in brain cortex-ablated cats. *Physiological Reports*. doi:10.14814/phy2.13458

Eaton RC, Lee RK, Foreman MB. 2001. The Mauthner cell and other identified neurons of the brainstem escape network of fish. *Prog Neurobiol* **63**:467–485.

Elliott P, Wallis DI, Foster GA, Stringer BM. 1999. Ionic mechanisms underlying excitatory effects of serotonin on embryonic rat motoneurons in long-term culture. *Neuroscience* **90**:1311–1323.

Ferreira-Pinto MJ, Ruder L, Capelli P, Arber S. 2018. Connecting Circuits for Supraspinal Control of Locomotion. *Neuron* **100**:361–374.

Gabriel JP, Ausborn J, Ampatzis K, Mahmood R, Eklöf-Ljunggren E, El Manira A. 2011. Principles governing recruitment of motoneurons during swimming in zebrafish. *Nat Neurosci* **14**:93.

Galassi M, Davies J, Theiler J, Gough B, Jungman G, Alken P, Booth M, Rossi F, Ulerich R. 2002. GNU scientific library. Network Theory Limited.

Gerkau NJ, Lerchundi R, Nelson JSE, Lantermann M, Meyer J, Hirrlinger J, Rose CR. 2019. Relation between activity-induced intracellular sodium transients and ATP dynamics in mouse hippocampal neurons. *J Physiol* **597**:5687–5705.

Getting PA. 1989. Emerging principles governing the operation of neural networks. *Annu Rev Neurosci* **12**:185–204.

Goldbeter A. 2018. Dissipative structures in biological systems: bistability, oscillations, spatial patterns and waves. *Philos Trans A Math Phys Eng Sci* **376**. doi:10.1098/rsta.2017.0376

Gonzalez-Islas C, Garcia-Bereguiain MA, Wenner P. 2020. Homeostatic Recovery of Embryonic Spinal Activity Initiated by Compensatory Changes in Resting Membrane Potential. *eNeuro* **7**. doi:10.1523/ENEURO.0526-19.2020

Gozal EA, O'Neill BE, Sawchuk MA, Zhu H, Halder M, Chou C-C, Hochman S. 2014. Anatomical and functional evidence for trace amines as unique modulators of locomotor function in the mammalian spinal cord. *Front Neural Circuits* **8**:134.

Gutierrez GJ, Marder E. 2014. Modulation of a Single Neuron Has State-Dependent Actions on Circuit Dynamics(,.). *eNeuro* **1**.

Gutierrez GJ, Marder E. 2013. Rectifying electrical synapses can affect the influence of synaptic modulation on output pattern robustness. *J Neurosci* **33**:13238–13248.

Gutierrez GJ, O'Leary T, Marder E. 2013. Multiple mechanisms switch an electrically coupled, synaptically inhibited neuron between competing rhythmic oscillators. *Neuron* **77**:845–858.

Guttman R, Feldman L, Jakobsson E. 1980. Frequency entrainment of squid axon membrane. *J Membr Biol* **56**:9–18.

Hachoumi L, Sillar KT. 2020. Developmental stage-dependent switching in the neuromodulation of vertebrate locomotor central pattern generator networks. *Dev Neurobiol* **80**:42–57.

Hao Z-Z, Spardy LE, Nguyen EBL, Rubin JE, Berkowitz A. 2011. Strong interactions between spinal cord networks for locomotion and scratching. *J Neurophysiol* **106**:1766–1781.

Hayes JA, Mendenhall JL, Brush BR, Del Negro CA. 2008. 4-Aminopyridine-sensitive outward currents in preBötzinger complex neurons influence respiratory rhythm generation in neonatal mice. *J Physiol* **586**:1921–1936.

Jasinski PE, Molkov YI, Shevtsova NA, Smith JC, Rybak IA. 2013. Sodium and calcium mechanisms of rhythmic bursting in excitatory neural networks of the pre-Bötzinger complex: a computational modelling study. *Eur J Neurosci* **37**:212–230.

Jha U, Thirumalai V. 2020. Neuromodulatory Selection of Motor Neuron Recruitment Patterns in a Visuomotor Behavior Increases Speed. *Curr Biol* **30**:788–801.e3.

Kim LH, Sharma S, Sharples SA, Mayr KA, Kwok CHT, Whelan PJ. 2017. Integration of Descending Command Systems for the Generation of Context-Specific Locomotor Behaviors. *Front Neurosci* **11**:581.

Kjaerulff O, Kiehn O. 2001. 5-HT modulation of multiple inward rectifiers in motoneurons in intact preparations of the neonatal rat spinal cord. *J Neurophysiol* **85**:580–593.

Koizumi H, Smith JC. 2008. Persistent Na+ and K+-dominated leak currents contribute to respiratory rhythm generation in the pre-Bötzinger complex in vitro. *J Neurosci* **28**:1773–1785.

Kristan WB Jr, Nusbaum MP. 1982. The dual role of serotonin in leech swimming. *J Physiol Paris* **78**:743–747.

Kueh D, Barnett WH, Cymbalyuk GS, Calabrese RL. 2016. Na(+)/K(+) pump interacts with the h-current to control bursting activity in central pattern generator neurons of leeches. *Elife* **5**. doi:10.7554/eLife.19322

Kuo JJ, Lee RH, Zhang L, Heckman CJ. 2006. Essential role of the persistent sodium current in spike initiation during slowly rising inputs in mouse spinal neurones. *J Physiol* **574**:819–834.

Lambert AM, Bonkowsky JL, Masino MA. 2012. The conserved dopaminergic diencephalospinal tract mediates vertebrate locomotor development in zebrafish larvae. *J Neurosci* **32**:13488–13500.

Lee RH, Heckman CJ. 1998. Bistability in spinal motoneurons in vivo: systematic variations in persistent inward currents. *J Neurophysiol* **80**:583–593.

Liao JC, Fetcho JR. 2008. Shared versus Specialized Glycinergic Spinal Interneurons in Axial Motor Circuits of Larval Zebrafish. *Journal of Neuroscience*. doi:10.1523/jneurosci.3330-08.2008

Li W-C, -C. Li W, Sautois B, Roberts A, Soffe SR. 2007. Reconfiguration of a Vertebrate Motor Network: Specific Neuron Recruitment and Context-Dependent Synaptic Plasticity. *Journal of Neuroscience* **27**:12267–12276.

Li X, Murray K, Harvey PJ, Ballou EW, Bennett DJ. 2007. Serotonin facilitates a persistent calcium current in motoneurons of rats with and without chronic spinal cord injury. *J Neurophysiol* **97**:1236–1246.

Mackie GO, Meech RW. 1985. Separate sodium and calcium spikes in the same axon. *Nature* **313**:791–793.

Malashchenko T, Barnett W, Burylko O, Cymbalyuk G. 2009. Control of bursting activity by modulation of ionic currents. *BMC Neuroscience*. doi:10.1186/1471-2202-10-s1-p27

Malashchenko T, Shilnikov A, Cymbalyuk G. 2011. Bistability of bursting and silence regimes in a model of a leech heart interneuron. *Phys Rev E Stat Nonlin Soft Matter Phys* **84**:041910.

Marcantoni M, Fuchs A, Löw P, Bartsch D, Kiehn O, Bellardita C. 2020. Early delivery and prolonged treatment with nimodipine prevents the development of spasticity after spinal cord injury in mice. *Sci Transl Med* **12**. doi:10.1126/scitranslmed.aay0167

Marchetti C, Nistri A. 2001. Neuronal bursting induced by NK3 receptor activation in the neonatal rat spinal cord in vitro. *J Neurophysiol* **86**:2939–2950.

Marder E, O'Leary T, Shruti S. 2014. Neuromodulation of circuits with variable parameters: single neurons and small circuits reveal principles of state-dependent and robust neuromodulation. *Annu Rev Neurosci* **37**:329–346.

Marin B, Barnett W, Doloc-Mihu A, Calabrese RL, Cymbalyuk G. 2011. Bringing rest into consideration: analyzing a database of computational models for multistability of oscillatory and stationary regimes. *BMC Neuroscience*. doi:10.1186/1471-2202-12-s1-p52

McDearmid JR, Drapeau P. 2006. Rhythmic motor activity evoked by NMDA in the spinal zebrafish larva. *J Neurophysiol* **95**:401–417.

McLean DL, Fan J, Higashijima S-I, Hale ME, Fetcho JR. 2007. A topographic map of recruitment in spinal cord. *Nature* **446**:71–75.

Meech RW, Thomas RC. 1977. The effect of calcium injection on the intracellular sodium and pH of snail neurones. *J Physiol* **265**:867–879.

Mor Y, Lev-Tov A. 2007. Analysis of rhythmic patterns produced by spinal neural networks. *J Neurophysiol* **98**:2807–2817.

Müller UK, Stamhuis EJ, Videler JJ. 2000. Hydrodynamics of unsteady fish swimming and the effects of body size: comparing the flow fields of fish larvae and adults. *J Exp Biol* **203**:193–206.

Parker J, Bondy B, Prilutsky BI, Cymbalyuk G. 2018. Control of transitions between locomotor-like and paw shake-like rhythms in a model of a multistable central pattern generator. *J Neurophysiol* **120**:1074–1089.

Parker J, Khwaja R, Cymbalyuk G. 2019. Asymmetric Control of Coexisting Slow and Fast Rhythms in a Multifunctional Central Pattern Generator: A Model Study. *Neurophysiology*. doi:10.1007/s11062-020-09834-9

Peck JH, Gaier E, Stevens E, Repicky S, Harris-Warrick RM. 2006. Amine modulation of Ih in a small neural network. *J Neurophysiol* **96**:2931–2940.

Picton LD, Nascimento F, Broadhead MJ, Sillar KT, Miles GB. 2017. Sodium Pumps Mediate Activity-Dependent Changes in Mammalian Motor Networks. *J Neurosci* **37**:906–921.

Picton LD, Sillar KT. 2016. Mechanisms underlying the endogenous dopaminergic inhibition of spinal locomotor circuit function in Xenopus tadpoles. *Sci Rep* **6**:35749.

Picton LD, Sillar KT, Zhang H-Y. 2018. Control of Xenopus Tadpole Locomotion via Selective Expression of Ih in Excitatory Interneurons. *Curr Biol* **28**:3911–3923.e2.

Prinz AA, Bucher D, Marder E. 2004. Similar network activity from disparate circuit parameters. *Nat Neurosci* **7**:1345–1352.

Puhl JG, Mesce KA. 2008. Dopamine activates the motor pattern for crawling in the medicinal leech. *J Neurosci* **28**:4192–4200.

Pujala A, Koyama M. 2019. Chronology-based architecture of descending circuits that underlie the development of locomotor repertoire after birth. *Elife* **8**. doi:10.7554/eLife.42135

Pulver SR, Griffith LC. 2010. Spike integration and cellular memory in a rhythmic network from Na+/K+ pump current dynamics. *Nat Neurosci* **13**:53–59.

Rybak IA, Shevtsova NA, Lafreniere-Roula M, McCrea DA. 2006. Modelling spinal circuitry involved in locomotor pattern generation: insights from deletions during fictive locomotion. *J Physiol* **577**:617–639.

Sharples SA, Humphreys JM, Jensen AM, Dhoopar S, Delaloye N, Clemens S, Whelan PJ. 2015. Dopaminergic modulation of locomotor network activity in the neonatal mouse spinal cord. *J Neurophysiol* **113**:2500–2510.

Sharples SA, Whelan PJ. 2017. Modulation of Rhythmic Activity in Mammalian Spinal Networks Is Dependent on Excitability State. *eNeuro* **4**. doi:10.1523/ENEURO.0368-16.2017

Sillar KT, Robertson RM. 2009. Thermal activation of escape swimming in post-hatching Xenopus laevis frog larvae. *J Exp Biol* **212**:2356–2364.

Smith M, Perrier J-F. 2006. Intrinsic properties shape the firing pattern of ventral horn interneurons from the spinal cord of the adult turtle. *J Neurophysiol* **96**:2670–2677.

Song J, Pallucchi I, Ausborn J, Ampatzis K, Bertuzzi M, Fontanel P, Picton LD, El Manira A. 2020. Multiple Rhythm-Generating Circuits Act in Tandem with Pacemaker Properties to Control the Start and Speed of Locomotion. *Neuron* **105**:1048–1061.e4.

Takahashi T. 1990. Inward rectification in neonatal rat spinal motoneurones. *J Physiol* **423**:47–62.

Talpalar AE, Kiehn O. 2010. Glutamatergic mechanisms for speed control and network operation in the rodent locomotor CpG. *Front Neural Circuits* **4**. doi:10.3389/fncir.2010.00019

Tazerart S, Viemari J-C, Darbon P, Vinay L, Brocard F. 2007. Contribution of persistent sodium current to locomotor pattern generation in neonatal rats. *J Neurophysiol* **98**:613–628.

Tazerart S, Vinay L, Brocard F. 2008. The persistent sodium current generates pacemaker activities in the central pattern generator for locomotion and regulates the locomotor rhythm. *J Neurosci* **28**:8577–8589.

Thoby-Brisson M, Ramirez J-M. 2000. Role of Inspiratory Pacemaker Neurons in Mediating the Hypoxic Response of the Respiratory NetworkIn Vitro. *The Journal of Neuroscience*. doi:10.1523/jneurosci.20-15-05858.2000

Tiwari MN, Mohan S, Biala Y, Yaari Y. 2018. Differential contributions of Ca -activated K channels and Na /K -ATPases to the generation of the slow afterhyperpolarization in CA1 pyramidal cells. *Hippocampus* **28**:338–357.

Tobin A-E, Calabrese RL. 2005. Myomodulin increases Ih and inhibits the NA/K pump to modulate bursting in leech heart interneurons. *J Neurophysiol* **94**:3938–3950.

Turrigiano GG, Marder E, Abbott LF. 1996. Cellular short-term memory from a slow potassium conductance. *J Neurophysiol* **75**:963–966.

Vargas A & Cymbalyuk G. 2019. Dynamics of the Na+/K+ pump and dopamine within a locomotor central pattern generator. Presented at the Society for Neuroscience.

Wang F, Smith NA, Xu Q, Fujita T, Baba A, Matsuda T, Takano T, Bekar L, Nedergaard M. 2012. Astrocytes modulate neural network activity by Ca^{2}+-dependent uptake of extracellular K+. *Sci Signal* **5**:ra26.

Whelan P, Bonnot A, O'Donovan MJ. 2000. Properties of rhythmic activity generated by the isolated spinal cord of the neonatal mouse. *J Neurophysiol* **84**:2821–2833.

Wiggin TD, Anderson TM, Eian J, Peck JH, Masino MA. 2012. Episodic swimming in the larval zebrafish is generated by a spatially distributed spinal network with modular functional organization. *J Neurophysiol* **108**:925–934.

Wiggin TD, Peck JH, Masino MA. 2014. Coordination of fictive motor activity in the larval zebrafish is generated by non-segmental mechanisms. *PLoS One* **9**:e109117.

Willard AL. 1981. Effects of serotonin on the generation of the motor program for swimming by the medicinal leech. *J Neurosci* **1**:936–944.

Wilson JM, Hartley R, Maxwell DJ, Todd AJ, Lieberam I, Kaltschmidt JA, Yoshida Y, Jessell TM, Brownstone RM. 2005. Conditional rhythmicity of ventral spinal interneurons defined by expression of the Hb9 homeodomain protein. *J Neurosci* **25**:5710–5719.

Wiltschko AB, Johnson MJ, Iurilli G, Peterson RE, Katon JM, Pashkovski SL, Abraira VE, Adams RP, Datta SR. 2015. Mapping Sub-Second Structure in Mouse Behavior. *Neuron* **88**:1121–1135.

Wotton CA, Cross CD, Bekar LK. 2020. Serotonin, norepinephrine, and acetylcholine differentially affect astrocytic potassium clearance to modulate somatosensory signaling in male mice. *J Neurosci Res* **98**:964–977.

Yang S-S, Li Y-C, Coley AA, Chamberlin LA, Yu P, Gao W-J. 2018. Cell-Type Specific Development of the Hyperpolarization-Activated Current, Ih, in Prefrontal Cortical Neurons. *Front Synaptic Neurosci* **10**:7.

Zhang H-Y, Picton L, Li W-C, Sillar KT. 2015. Mechanisms underlying the activity-dependent regulation of locomotor network performance by the Na+ pump. *Sci Rep* **5**:16188.

Zhang H-Y, Sillar KT. 2012. Short-term memory of motor network performance via activity-dependent potentiation of Na+/K+ pump function. *Curr Biol* **22**:526–531.

Zhang Y, Bucher D, Nadim F. 2017. Ionic mechanisms underlying history-dependence of conduction delay in an unmyelinated axon. *eLife*. doi:10.7554/elife.25382

Zhang Y, Narayan S, Geiman E, Lanuza GM, Velasquez T, Shanks B, Akay T, Dyck J, Pearson K, Gosgnach S, Fan C-M, Goulding M. 2008. V3 Spinal Neurons Establish a Robust and Balanced Locomotor Rhythm during Walking. *Neuron* **60**:84–96.

Zhong G, Masino MA, Harris-Warrick RM. 2007. Persistent Sodium Currents Participate in Fictive Locomotion Generation in Neonatal Mouse Spinal Cord. *Journal of Neuroscience* **27**:4507–4518.

Methods

Ethical approval & animals

Experiments were performed on neonatal C57BL/6 (n = 50) mice, postnatal 0–4 days old (P0–P4). The University of Calgary Health Sciences Animal Care Committee approved all procedures (protocol number AC16-0182).

Tissue preparation

We anesthetized the animals via hypothermia by placing them at −20 °C for 5–10 minutes. Animals were then decapitated, eviscerated, and the spinal column was pinned ventral side up in a dissecting dish lined with silicone elastomer (Sylgard, MilliporeSigma, Oakville, ON, Canada) and superfused with room temperature (21 ºC) carbogenated (95% O_2-5% CO_2) artificial cerebrospinal fluid (aCSF; in mM, 128 NaCl, 4 KCl, 1 $MgSO_4$, 1.5 $CaCl_2$, 0.5 Na_2HPO_4, 21 $NaHCO_3$, 30 D-glucose; total osmolarity: 310–315 mOsm). The spinal cord was isolated by performing a ventral laminectomy. The nerve roots connecting the spinal cord to the vertebral column were subsequently cut, isolating the spinal cord. We then transferred the isolated spinal cord to a recording chamber perfused with carbogenated aCSF and placed it ventral side up. We gradually increased the bath temperature to 27 °C (Whelan et al., 2000). The advantage of this method is that it is close to physiological temperature and avoids fluctuations in room temperature. We left the spinal cords to stabilize for 1 hour before performing experiments.

Electrophysiology

Extracellular electrophysiological recordings were obtained from ventral roots with tight-fitting suction electrodes fashioned from polyethylene tubing (PE50). Total signal amplification was 1000×, including a pre-amplifier (10×) and second stage amplifiers (Cornerstone EX4-400 Quad Differential Amplifier) at 100×. Amplified signals were acquired in DC and digitized at 2.5 KHz (Digidata

1440A/1550B; Molecular Devices; Sunnyvale, CA). We saved data acquired using Clampex 10.7 software (Molecular Devices) to a desktop computer for offline analysis.

Pharmacology

Episodic rhythmicity was evoked by bath application of dopamine hydrochloride (50 µM; Sigma-Aldrich). We blocked the I_{Pump} with ouabain (100 nM-1 µM; Tocris), I_h - producing hyperpolarization-activated cyclic nucleotide (HCN) channels with ZD 7288 (30–50 µM; Tocris), and deployed nimodipine (15 µM; Tocris) and the $NaV_{1.6}$ blocker 4,9 Anhydro-tetrodotoxin (100–200 nM; Tocris) to block calcium and Na^+-dependent pacemaker properties, respectively. All pharmacological agents were prepared following solubility guidelines specified by their respective vendors. We were careful to ensure that volumes of drugs prepared in dimethyl sulfoxide (DMSO) did not exceed 0.04% (vol/vol) concentration in working solutions.

Computational model

The model consists of two identical and mutually inhibitory neurons, which represents one side, flexor and extensor, of a spinal CPG as an HCO. Each neuron, described by a single equipotential compartment, represents the activity of a population (flexor or extensor) of controlling interneurons. Each neuron is equipped with ionic currents modelled using Hodgkin-Huxley formalism: slowly inactivating persistent Na^+ current (I_{NaP}), hyperpolarization-activated inward (h-) current (I_h), and an inhibitory spike-mediated synaptic current (I_{Syn}), low-threshold slowly inactivating Ca^{2+} current (I_{CaS}), a fast Na^+ current (I_{NaF}), a delayed rectifier-like K^+ current (I_{KDR}), and a fast transient K^+ current (I_{KA}). I_{KA} was implemented using experimental data from previous models (Hayes et al., 2008). It's activation variable is fast and is implemented as instantaneous. The equations for I_{NaF} and I_{KDR} were obtained from earlier work (Rybak et al., 2006) and implemented along with I_{CaS}, I_{Syn}, and I_{NaP} described in (Bondy et al., 2016; Parker et al. 2018). Our descriptions of I_h and leak currents were adapted from our previous study (Kueh et al., 2016) and had corresponding reversal potentials for Na^+ and K^+ components. The components of I_h shared the same conductance and activation values, but conductance was scaled differently, with 3/7 and 4/7 for the Na^+ and K^+ components, respectively.

The membrane potential of each neuron in the HCO is governed by the following current conservation equation:

$$C\frac{dV_m}{dt} = -[I_{NaF} + I_{NaP} + I_{KDR} + I_{KA} + I_{h-Na} + I_{h-K} + I_{CaS} + I_{L-Na} + I_{L-K} + I_{Pump} + I_{Syn} + I_{PulseExc} + I_{PulseInh}]$$

where C is the membrane capacitance in nF, V_m is the membrane potential in mV, and t is time in seconds, and I_{xyz} are ionic membrane currents: They are described by the following formula:

$I_{NaF} = \bar{g}_{NaF}\mathrm{m}^3_{\mathrm{NaF}\infty}(V_m)\mathrm{h}_{\mathrm{NaF}}[\mathrm{V_m} - \mathrm{E_{Na}}]$, $I_{NaP} = \bar{g}_{NaP}m_{NaP}h_{NaP}[V_m - E_{Na}]$,

$I_{KDR} = \bar{g}_{KDR}\, m^4_{KDR}[V_m - E_K]$, $I_{KA} = \bar{g}_{KA}m_{KA\infty}(V_m)h_{KA}[V_m - E_K]$,

$I_{h-Na} = \frac{3}{7}\bar{g}_h m_h^2[V_m - E_{Na}]$,

$I_{h-K} = \frac{4}{7}\bar{g}_h m_h^2[V_m - E_K]$,

$I_{CaS} = \bar{g}_{CaS}\, m_{CaS}^3 h_{CaS}[V_m - E_{Ca}]$

and two components of the leak current:

$$I_{L-Na} = g_{L-Na}[V_m - E_{Na}]$$

$$I_{L-K} = g_{L-K}[V_m - E_K]$$

where leak conductances were computed with the reference values of equivalent total leak conductance g_L and reversal potential E_{LRef} using the Na^+ reversal potential:

E_{NaRef} : $g_{L-Na} = g_L \frac{[E_{LRef}-E_K]}{[E_{NaRef}-E_K]}$ and $g_{L-K} = g_L \frac{[E_{LRef}-E_{NaRef}]}{[E_K-E_{NaRef}]}$.

The description of the pump current was adapted from Cressman et al. (2009); it has maximal value $I_{PumpMax}$ and is activated by $[Na]_i$ and $[K]_o$ with concentrations of half-activation 25 mM and 6 mM, respectively:

$I_{Pump} = \frac{I_{PumpMax}}{[1+\exp((25-[Na]_i)/3)]*[1+\exp(6-[K]_e)]}$.

I_{Syn} is the synaptic current:

$$I_{Syn} = \bar{g}_{Syn}\, \mathrm{m}_{SynPre}\ (V_m - E_{Syn})$$

where m_{SynPre} is a synaptic activation variable of the presynaptic cell. $I_{PulseExc}$ and $I_{PulseInh}$ are injected excitatory and inhibitory currents, respectively: $I_{PulseExc} = \bar{g}_{Pulse}\ (V_m - E_{Exc})$ and $I_{PulseInh} = \bar{g}_{Pulse}\ (V_m - E_{Inh})$ with $E_{Exc} = 0\ mV$ and $E_{Inh} = -75\ mV$. They are injected as short pulses to perturb the model, by setting $\bar{g}_{Pulse} = 35.5\ nS$ during the pulse and $\bar{g}_{Pulse} = 0\ nS$, otherwise. The gating variable are governed by the following equations:

$$\frac{dh_{NaF}}{dt} = (\mathrm{f}_\infty(7, -29, V_m) - h_{NaF})/\tau_{h_{NaF}}$$

$$\frac{dm_{NaP}}{dt} = (\mathrm{f}_\infty(-4.1, -43, V_m) - m_{NaP})\ /0.001$$

$$\frac{dh_{NaP}}{dt} = (\mathrm{f}_\infty(5, -57, V_m) - h_{NaP})\ /0.1$$

$$\frac{dm_{KDR}}{dt} = (\mathrm{f}_\infty(-15, -18, V_m) - m_{KDR})\,/\tau_{m_{KDR}}$$

$$\frac{dh_{KA}}{dt} = (\mathrm{f}_\infty(5, -59.8, V_m) - h_{KA})/0.02$$

$$\frac{dm_{CaS}}{dt} = (\mathrm{f}_\infty(-4.27, -45.46, V_m) - m_{CaS})/\tau_{\mathrm{m}_{CaS}}$$

$$\frac{dh_{CaS}}{dt} = (\mathrm{f}_\infty(0.75, -57.3, V_m) - h_{CaS})/0.485$$

$$\frac{dm_h}{dt} = \left(\frac{1}{1 + 2\exp\left(221.4(V_m - V_{\frac{1}{2}m_h})\right) + \exp\left(615(V_m - V_{\frac{1}{2}m_h})\right)} - m_h\right)/\tau_h$$

$$\frac{\mathrm{dm}_{Syn}}{dt} = (\mathrm{f}_\infty(-0.4, -25, V_m) - \mathrm{m}_{Syn})/0.05$$

where $\mathrm{f}_\infty(\mathrm{a}, V_{\frac{1}{2}}, V_m) = \frac{1}{1+\exp\left(\frac{V_m - V_{\frac{1}{2}}}{a}\right)}$, $\mathrm{m}_{\mathrm{NaF}\infty}(V_m) = \mathrm{f}_\infty(-7.8, -18, V_m)$,

$\mathrm{m}_{\mathrm{KA}\infty}(V_m) = \mathrm{f}_\infty(-10, -20, V_m)$, $\tau_{h_{NaF}} = \frac{0.03}{\exp\left(\frac{V_m+46}{15}\right)+\exp\left(\frac{V_m+46}{-16}\right)}$, $\tau_{m_{KDR}} = \frac{0.007}{\exp\left(\frac{V_m-7}{40}\right)+\exp\left(\frac{V_m-7}{-50}\right)}$,

$\tau_{\mathrm{m}_{CaS}} = \frac{0.001}{\frac{0.02(V_m+47.87)}{1+\exp\left(\frac{V_m+47.87}{-4.5}\right)}+\frac{-0.05(V_m+50.87)}{1+\exp\left(\frac{V_m+50.87}{4.5}\right)}}$, $\tau_h = \frac{1}{0.5+\frac{1.7}{1+\exp(-100(V_m+73))}}$

Intracellular potassium concentrations ($[K]_i$) and extracellular potassium concentration ($[K]_o$) are fixed parameters. Our model has dynamic intracellular Na^+ concentration ($[Na]_i$) and fixed extracellular Na^+ concentration ($[Na]_o$). To compute $[Na]_i$, the model accounts for Na^+ influx carried by the Na^+ currents (I_{NaP} and I_{NaF}) and Na^+ components of leak (I_{L-Na}) and h- (I_{h-Na}) currents, and outflux produced by the Na^+/K^+ ATPase pump current (I_{Pump}):

$$\frac{d[Na]_i}{dt} = -\alpha\left(I_{h-Na} + I_{L-Na} + I_{NaF} + I_{NaP} + 3I_{Pump}\right)$$

where $\alpha = \frac{1}{vF} = 4.682255338155292$ mM/pA/s, v is intracellular volume and F is the Faraday's constant. Reversal potentials for Na^+ and K^+ currents are computed as the Nernst potentials $E_{Na} = \frac{RT}{F} ln \frac{[Na]_e}{[Na]_i}$ and $E_K = \frac{RT}{F} ln \frac{[K]_e}{[K]_i}$ with $\frac{RT}{F} = 26.45$ mV, using fixed $[Na]_e = 120\,mM$, computed state variable $[Na]_i$, and fixed $[K]_e = 9$ mM and $[K]_i = 130$ mM. Canonical values of other model parameters are $C = 0.001$ nF, $\bar{g}_{NaF} = 106$ nS, $\bar{g}_{NaP} = 5$ nS, $\bar{g}_{KDR} = 62$ nS, $\bar{g}_{KA} = 1.15\,nS$, $\bar{g}_h =$

0.2645 nS, $\bar{g}_{CaS} = 2.265$ nS , $E_{Ca} = 160$ mV, $g_L = 1.825$ nS , $E_{LRef} = -55\ mV$, $E_{NaRef} = 65$ mV, $\bar{g}_{Syn} = 0.1$ nS, $E_{Syn} = -75$ mV.

Data analysis

The model was implemented in C programming language and analyzed data using MATLAB (Mathworks Inc, Natick, MA.). Integration was performed using the explicit embedded Runge-Kutta Prince-Dormand (8,9) method with an absolute error tolerance of 10^{-8}, relative error tolerance of 10^{-9}, and an initial step size of 10^{-8} (the GNU scientific library; Galassi et al., 2002). Investigation of the model through parameter sweeps used the last point from the previous parameter value as the initial condition for the new parameter value.

Episodes of rhythmicity were analyzed using custom-written MATLAB scripts to detect episode onset, offset, and amplitude. We determined episode onset and offset from DC signals that were detrended, band-pass filtered (0.01–1 Hz), and smoothed with a Gaussian-weighted moving average. Peak amplitude of each detected episode was extracted from raw, unprocessed signal. We then calculated EP, ED, lag time, and phase in Excel from episode onset and offset times. The EP coefficient of variation (EP-CV) was set to distinguish regular (> 0.2) and irregular (< 0.2) patterns of episodic bursting.

Statistical analysis

We analyzed changes in parameters of episodic rhythmicity recorded in ventral roots over time using one-way or two-way repeated measures analyses of variance (ANOVA), as appropriate. Pharmacological manipulations of spinal circuits were compared to appropriate time-matched preparations using unpaired t-tests. Data that violated assumptions of normality (Shapiro–Wilk test) or equal variance (Brown–Forsythe test) were analyzed via nonparametric Mann–Whitney *U* (if two groups) or Kruskal–Wallis (if more than two groups) tests. All effects surpassing a significance threshold of $p < 0.05$ were further examined with Holm-Sidak post hoc tests to compare all treatment conditions to the appropriate normalized time-matched vehicle control.

Supplemental Material

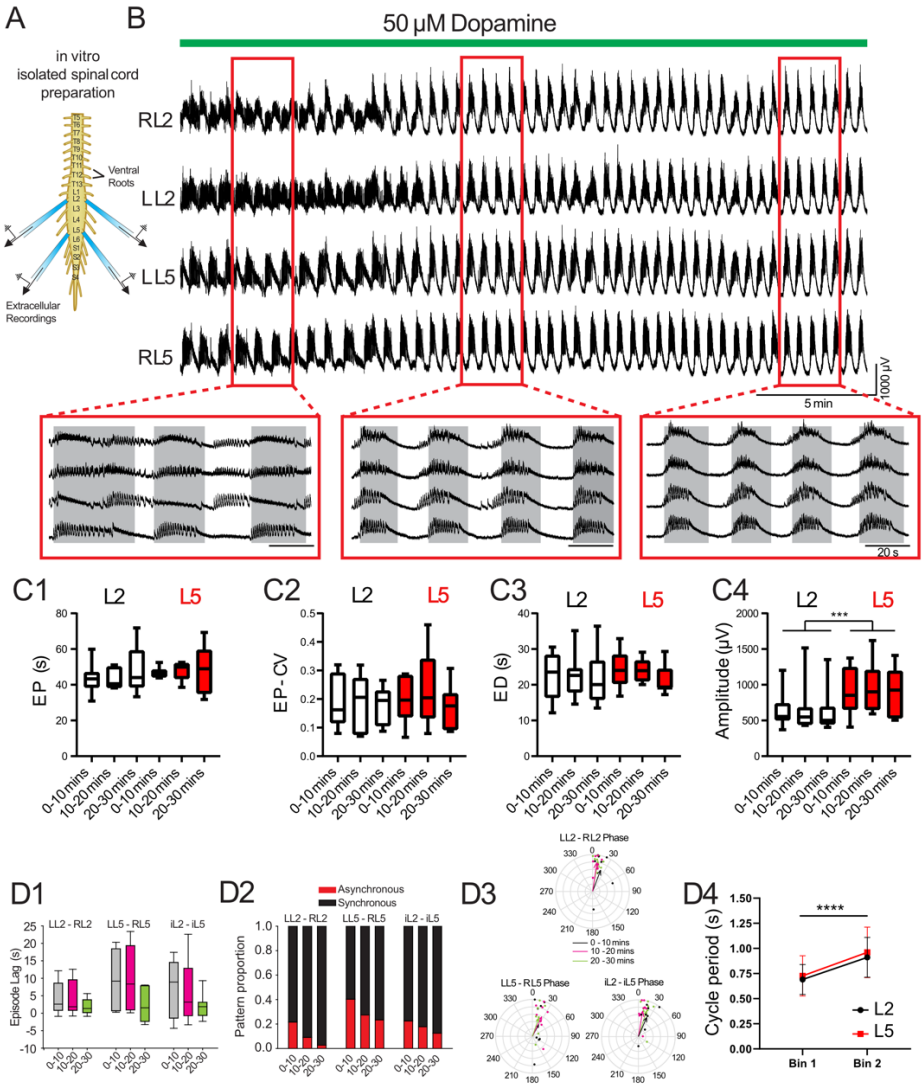

Supplemental Figure 1: Detailed analysis of dopamine-evoked rhythmicity. (A) Suction electrodes were used to record extracellular neurograms from left (L) and right (R) ventral roots of the second (L2) and fifth (L5) lumbar segments. (B) Dopamine applied at 50 μM (green bar) evoked episodic rhythmicity in lumbar spinal circuits. Expanded red boxes highlight changes in episode patterning across ventral roots over time. (C) From 0-30 minutes after dopamine application, episodes did not differ between L2 and L5 in episode period (EP: C1), episode period coefficient of variation (EP - CV: C2) or episode duration (ED: C3). Episodes had significantly higher amplitudes in L5 compared to L2 at all time points (C4). Box and whisker plots display interquartile range (boxes), median (horizontal black lines), maximum, and minimum values in data range (whiskers). (D1) The average episode onset lag times did not differ between root pairs or overtime (0-30 mins) when considering group data (n=8). (D2) Phase analysis for individual episodes from eight preparations revealed that the majority of episodes tended toward synchrony (phase between 0 - 90 degrees) (black bars), however there was a greater proportion of episodes that tended toward asynchrony (phase between 90 - 180 degrees)(red bars) in the left-right L5 ventral root pair than in the left-right L2 and ipsilateral L2-L5 pairs. The proportion of asynchronous episodes decreased in all root pairs over time. (D3) Phase plots illustrate mean phase relationships for left-right L2, L5 and ipsilateral L2-L2 pairs across all episodes over time (black: 0-10 mins; pink; 10-20 min; green; 20-30 mins). Phase plots were analyzed with Rayleigh Statistics. (D4) The cycle period of the intra-episode rhythm increased between the first (bin 1) and second (bin 2) halves of an episode. Data in D4 are presented as mean ± SD during the first (Bin 1) and second (Bin 2) half of each episode. Asterisks denote significance (*** $p < 0.001$, **** $p<0.0001$) from post hoc analyses following a 2-way ANOVA.

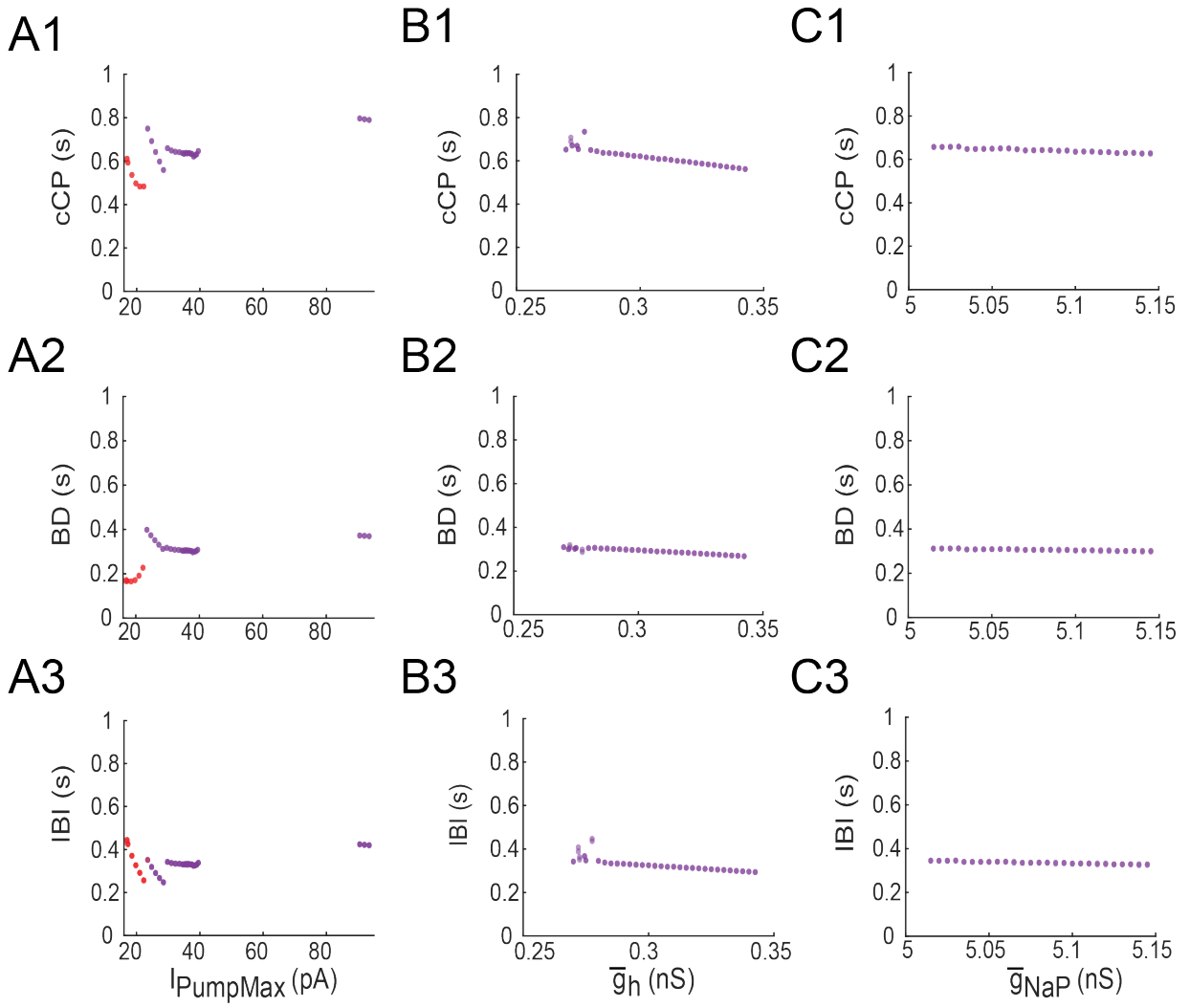

Supplemental Figure 2: Rhythm parameters for continuous bursting in response to manipulation of $I_{PumpMax}$, $\bar{g}_h$, and $\bar{g}_{NaP}$ (A1) Depicts changes in cycle period (cCP) for continuous bursting for different values of $I_{PumpMax}$. The transition between plateau and functional bursting occurred near 25 pA. The second jump in cCP was due to changes in interburst interval (IBI). The model transitioned once more to continuous bursting with a consistent, higher cycle period. (A2) Shows changes in burst duration (BD) in continuous patterns as $I_{PumpMax}$ varied. The low burst duration seen from 16.85 pA to approximately 25 pA reflects nonfunctional plateau bursting. Once functional bursting began, burst duration decreased and then the model transitioned to episodic bursting. The second time the model transitioned to continuous bursting, BD increased. (A3) shows IBI for continuous patterns as $I_{PumpMax}$ was swept. At the onset of plateau bursting, IBI decreased before a transition to functional bursting, and then jumped higher. IBI then decreased with higher pump strength before jumping up again within the functional bursting pattern, then remained relatively consistent before transitioning to episodic bursting. When the model again transitioned to continuous bursting, IBI was also higher and changed very little as pump strength increased. (B1) The cCP for the continuous pattern changed very little with changes in $\bar{g}_{NaP}$, slightly decreasing throughout the continuous pattern. (B2) The BD within continuous patterns was also very consistent, decreasing slowly as $\bar{g}_{NaP}$ increased. (B3) The IBI for continuous patterns was very consistent as $\bar{g}_{NaP}$ was swept, decreasing slowly as $\bar{g}_{NaP}$ increased. (C1) As $\bar{g}_h$ changed, cCP for continuous patterns was initially highly variable after the model transitioned from episodic bursting. When this variability subsided, cCP decreased as $\bar{g}_h$ increased. (C2) depicts BD within continuous patterns as $\bar{g}_h$ varied. BD showed less variability after the transition and slowly decreased as $\bar{g}_h$ increased. (C3) As $\bar{g}_h$ was swept, the IBI for continuous patterns was variable after the transition, before consistently decreasing as $\bar{g}_h$ increased.

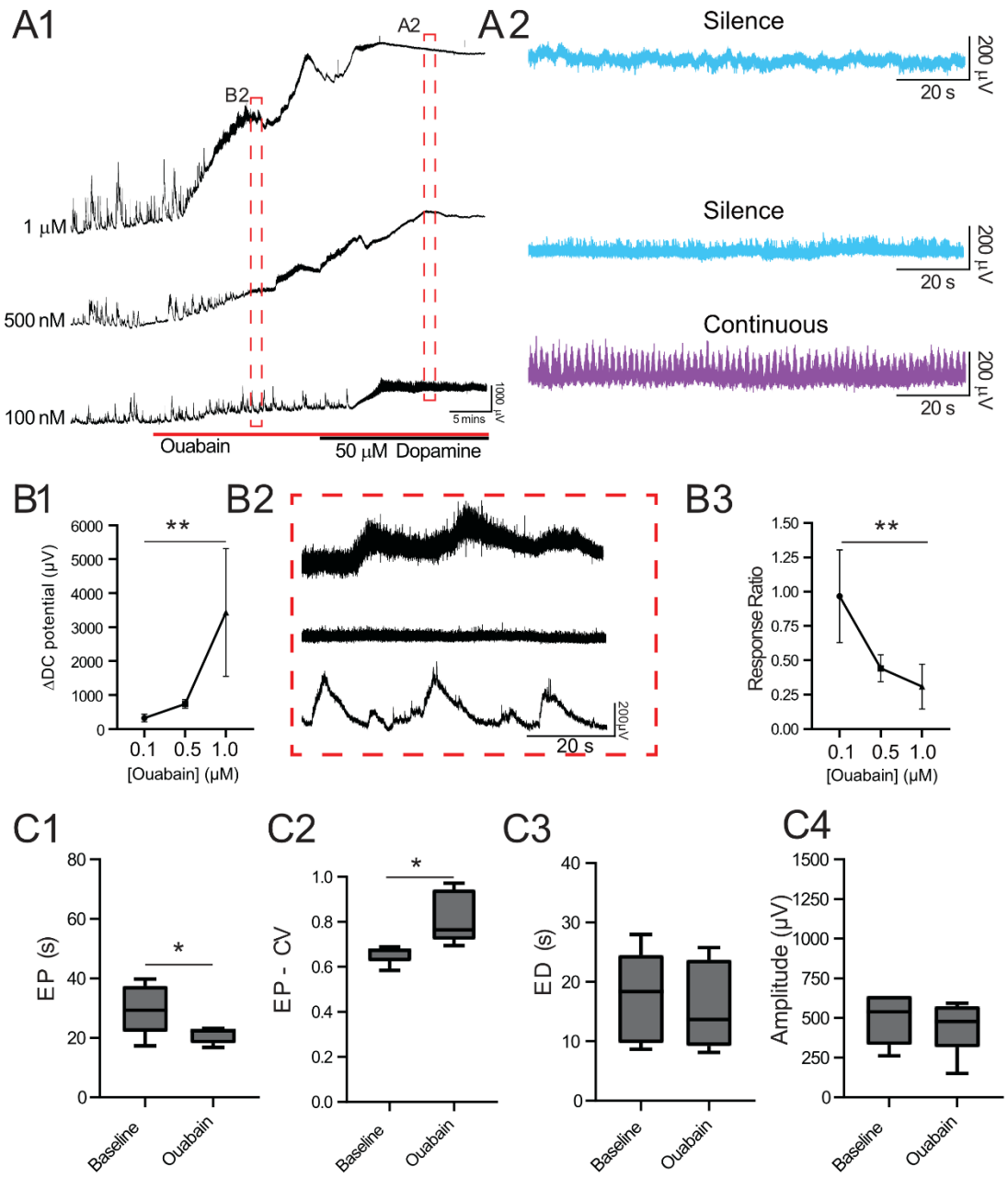

Supplemental Figure 3: Dose response for ouabain on spinal network activity. (A1) Displays extracellular neurograms of spontaneous activity recorded in DC from ventral roots during application of 1 μM (n = 6), 500 nM (n = 2), and 100 nM (n = 6) of ouabain (red bar) and subsequent application of dopamine (50 μM: black bar). (A2) Neurograms displaying network activity elicited by dopamine in the presence of different concentrations of ouabain highlighted in A1. (B1) Ouabain depolarized the DC potential of ventral root neurograms. Data are presented as mean ± SD change in DC potential. Traces in B2 represent expanded segments of spontaneous activity in the presence of different concentrations of ouabain, defined by red dashed boxes in A1. They highlight the suppression of spontaneous network activity at higher concentrations (500 nM and 1 μM). The suppression is indicated by the significant reduction in response ratio. The response ratio (B3) was calculated by dividing the root mean square of activity across a 5-minute epoch in the presence of ouabain by their respective baselines during a 5-minute epoch prior to ouabain application. 100 nM ouabain (n = 6) significantly reduced the spontaneous episode period (EP; C1), increased the episode period coefficient of variation (EP – CV; C2), but did not alter the duration (ED: C3) or amplitude (C4) of spontaneous episodes, compared to baseline. Box and whisker plots display interquartile range (boxes), median (horizontal black lines), maximum, and minimum value in data range (whiskers). Asterisks denote significance level following paired t-tests (*$p < 0.05$, **$p < 0.01$.).

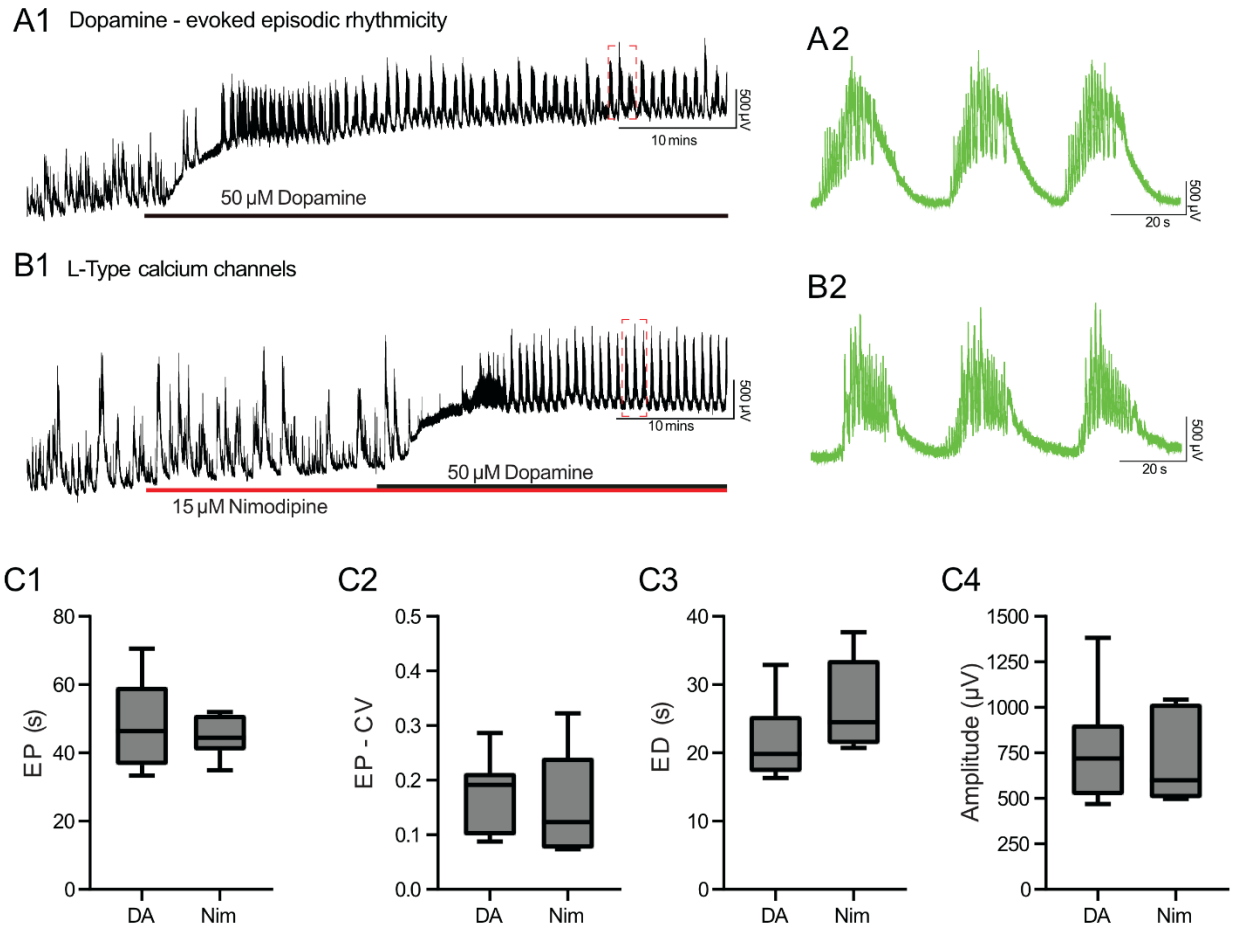

Supplemental Figure 4: L-type calcium channels contribute minimally to episodic rhythmicity

(A1–A2) We measured episodic rhythmicity evoked by dopamine (A1 black bars) in the presence of the nimodipine (red bar; B1–B2). Traces in A2 and B2 represent expanded segments defined by red dashed boxes in A1 and B1, respectively. Nimodipine did not alter the episode period (EP; C1), episode period coefficient of variation (EP-CV; C2), episode duration (ED; C3), or amplitude (C4) of dopamine-evoked episodes. Box and whisker plots display interquartile range (boxes), median (horizontal black lines), maximum, and minimum value in data range (whiskers) for episodic rhythms evoked by dopamine alone (n = 8) or in the presence of nimodipine (n = 6) in separate sets of experiments and were compared using unpaired t-tests.